Shear localization and its impact on mass-transport complexes seal potential: insights from geophysical datasets

Zhenghao Han[1], Nan Wu[1*], Jinfeng Ren[2,3], Zenggui Kuang [2,3]

[1]State Key Laboratory of Marine Geology, Tongji University, 1239 Siping Road, Shanghai, 200092, China

[2]National Engineering Research Center of Gas Hydrate Exploration and Development, Guangzhou Marine Geological Survey, Guangzhou, 511458, China

[3]Key Laboratory of Marine Mineral Resources, Ministry of Natural Resources, Guangzhou, 510075, China

*Nan Wu (nanwu@tongji.edu.cn)

Abstract

Mass-transport complexes (MTCs), the deposits of submarine slope failures and common features of sedimentary basins worldwide, can act as effective seals for hydrocarbons and carbon sequestration due to shear-induced overcompaction. However, seal failure is occasionally observed in specific parts of MTCs, leading to hydrocarbon and carbon dioxide leakage, and posing potential threats to seabed stability. In this study, we combine 3D seismic and well log data from Qiongdongnan Basin, northern South China Sea, to investigate the mechanisms that influence and control the seal potential of MTCs. We identified three vertically stacked MTCs overlying a gas hydrate bearing interval. Seismic interpretation reveals that MTCs seal tends to fail in intervals where MTCs overlies the frontal ramp or remnant block, whereas the remaining intervals effectively seal the underlying gas hydrate. Petrophysical analyses show that MTCs intervals overlying frontal ramps or remnant blocks exhibit significantly lower density and velocity, higher porosity and permeability, indicating reduced compaction in these intervals. Numerical simulations indicate that during MTCs emplacement, shear localization normally develops in the lowermost part, forming a narrow (10~20% MTCs total thickness), highly deformed basal shear zone. However, shear localization is disrupted by the remnant block or frontal ramp, leading to low shear strain and thus low seal potential in MTCs intervals overlying the remnant block or frontal ramp. Therefore, we propose that shear localization is a key mechanism controlling the seal potential of MTCs. Disruption of this process during emplacement can significantly compromise MTCs seal potential, with important implications for understanding

hydrocarbon distribution and for assessing the feasibility of submarine carbon sequestration using MTCs as natural seals.

1 Introduction

Mass-transport complexes (MTCs) are intensely deformed sedimentary bodies generated by the downslope movement of unstable sediments under gravity (Talling et al., 2007; Bull et al., 2009; Wu et al., 2024). MTCs can cover areas ranging from a few square kilometers to over ten thousand square kilometers, with volumes reaching up to several hundred cubic kilometers (Karstens et al., 2023; Richardson et al., 2011; Lenz & Sawyer, 2022). Borehole-based studies indicate that mud-rich MTCs typically exhibit increased resistivity, P-wave velocity, and density, along with reduced porosity and water content compared to the surrounding strata (Dugan et al., 2012; Wu et al., 2021; Wu et al., 2022). Additionally, the lower intervals of mud-rich MTCs are characterized by the highest P-wave velocity and density along with the lowest porosity, representing the most compacted interval named basal shear zone (Wu et al., 2021). In contrast, the internal sand-rich blocks typically exhibit lower P-wave velocity and density, higher porosity and permeability compared to the surrounding matrix, suggesting that they may maintain high reservoir space (Cox et al., 2020; Wu et al., 2021). Therefore, MTCs and their basal shear zones are considered effective seals for hydrocarbons, while the sand-rich blocks are considered potential reservoirs.

Although MTCs are generally considered effective hydrocarbon seals due to their high compaction and low permeability, recent studies have shown that seal failure may occur in specific parts of MTCs. For example, fluid escape features such as pockmarks, gas chimneys, and acoustic anomalies are observed within MTCs, indicating vertical fluid migration and local seal failure (Lastras et al., 2004; Noda et al., 2013; Pattier et al., 2013). The apparent contradiction between the compacted, low-permeability nature of MTCs and the observed indicators of fluid migration prompts an important question: when do MTCs serve as effective seals, and what conditions lead to their failure? To address the above question, we focus on the Songnan Low Uplift region in the Qiongdongnan Basin, South

China Sea, where vertically stacked MTCs overlying gas hydrate-bearing layers have been repeatedly breached by fluid migration (Yang et al., 2013; Kuang et al., 2023). We integrate 3D seismic reflection and well log data to characterize MTCs morphological features and petrophysical properties, and ultimately to identify the key factors that control their seal potential. We follow the seminal definitions by Kaldi and Atkinson (1997), in which seal potential is defined as a combination of seal capacity (the hydrocarbon column height that can physically be held back), seal geometry (areal extent and thickness), and seal integrity (rock mechanical properties).

Our results reveal that during emplacement, MTCs are subject to a strain-focusing mechanism known as shear localization. This process typically occurs along the basal interval and gives rise to a highly deformed band that corresponds to the basal shear zone previously identified by Wu et al. (2021), which plays a key role in controlling the mechanical and sealing behavior of MTCs. Intervals of the in-situ strata in our study area were strengthened prior to MTCs emplacement by gas hydrate cementation or sandy turbidite infilling. These mechanically strengthened layers resisted erosion during downslope emplacement of the MTC, forcing the moving mass to ramp up them and leaving the uneroded strata as remnant blocks or frontal ramps. Where such structures were encountered, shear localization became disrupted and strain was reduced. As a result, the overlying intervals of the MTCs underwent markedly reduced shear compaction, developing higher porosity, permeability and therefore exhibiting significantly lower seal potential. Understanding the conditions when MTCs maintain or lose their seal potential is critical for evaluating subsurface fluid migration pathways, hydrocarbon trap integrity, and gas hydrate system evolution in deep-water basins. These insights also aid in evaluating gas hydrate reservoirs and guiding site selection for future carbon sequestration using MTCs as natural seals.

2 Geological Setting

Qiongdongnan Basin is a Cenozoic rift basin characterized by thick Paleogene to Quaternary sediments (6000~12,000 m) situated atop a Mesozoic igneous basement in the northern South China

Sea (Huang et al., 2016). Due to regional erosion caused by the uplift of the Tibetan Plateau and the associated East Asia monsoon, substantial volumes of siliceous sediment are transported from the southwestern Yangtze Block through the Red River system with additional sources from eastern Indochina Block and Hainan (Figure 1a; Su et al., 2019).

Multiple phases of rifting and post-rift thermal subsidence have shaped the basin, forming a complex network of normal faults and fracture zones (Yang et al., 2022). These faults act as major conduits for vertical fluid migration, as evidenced by the widespread development of gas chimneys and fault-rooted seepage structures (Cartwright & Santamarina, 2015; Kuang et al., 2023; Serov et al., 2023). Focused fluid flow along these faults promotes gas hydrate formation and overpressure buildup within sediments, both of which contribute to reduced slope stability (Mountjoy et al., 2014; Omosanya 2018; Wu et al., 2020). The interplay between high sedimentation rates, active faulting, and intense fluid activity in the Qiongdongnan Basin thus creates favorable conditions for submarine slope failure and the development of MTCs.

The study area specifically focuses on the Songnan Low Uplift within the Qiongdongnan Basin, which encompasses key zones targeted for gas hydrate exploration in the South China Sea (Figure 1b). Since 2013, the Guangzhou Marine Geological Survey has identified multiple conventional gas fields and gas hydrate reservoirs in the Qiongdongnan Basin (Figure 1b). Seismic and well log data suggest that MTCs are widely developed in the Songnan Low Uplift and often occur in close spatial association with gas hydrate-bearing intervals (Kuang et al., 2023; Ren et al., 2024). This spatial configuration implies a possible sealing relationship between MTCs and the gas hydrate beneath them.

3 Data and Methods

3.1 Seismic data and well log data

We use 3D seismic data provided by Guangzhou Marine Geological Survey. The 3D seismic data were collected from the Songnan Low Uplift region in 2018, covering an area of approximately 360 km² with water depths ranging from 1,650 to 1,800 m (Figure 1b). The 3D seismic data are post-stack

time-migrated and zero-phase processed with positive amplitudes represented by a red and yellow peak and negative amplitudes represented by a blue and grey trough (Figure 2). The 3D seismic surveys have a dominant frequency of 40 Hz and an average seismic velocity of 1,660 m/s near the seabed sediment, which gives an approximate vertical resolution of c. 10 m for the near seabed sediments.

The well log data were acquired using Schlumberger tools from four wells (W1, W2, W3, W4), including density, resistivity, neutron, acoustic, nuclear magnetic measurements, and in-situ temperature measurements (Figure 1b). To establish the relationship between depth domain (true vertical depth; TVD) well log data and time domain (two-way traveltime; TWT) seismic data, seismic-well tie is performed respectively for each well. Seismic-well tie begins with creating a synthetic seismogram using sonic and density logs to simulate how seismic waves travel through subsurface geobodies at the well site (Lines & Newrick, 2004). This synthetic seismogram is then compared to the actual seismic data collected near the well. By aligning the synthetic seismogram with the actual seismic trace, we can ensure that seismic reflections accurately match the geological layers observed in the well, enhancing the reliability of subsurface interpretations (see **Appendix A** for details).

3.2 Seismic attributes analysis

Seismic attributes are quantitative measurements derived from seismic data to reveal subsurface structures and properties that may not be immediately apparent in raw datasets (Chopra & Marfurt, 2007). In this study, we use variance and spectral decomposition with RGB blending to enhance the interpretation of complex geological features such as MTCs and fluid escape pipes.

The variance attribute measures the variability or heterogeneity within seismic traces, making it ideal for highlighting discontinuities (Chopra & Marfurt, 2007). For MTCs, high variance often corresponds to chaotic zones caused by sediment mixing during transport (Chopra & Marfurt, 2007; Chen et al., 2022). For fluid escape pipes, these features create vertical disturbances in seismic data,

which manifest as zones of high variance (Cartwright et al., 2007; Cartwright & Santamarina, 2015). By applying variance attribute, we identify the spatial extent, boundaries, internal architecture of MTCs and enhance the visibility of fluid escape pipes.

Spectral decomposition is a frequency based seismic attribute analysis technique that breaks down seismic data into its individual frequency components (Anomneze et al., 2025). RGB blending is a visualization technique that builds on spectral decomposition to create an intuitive representation of frequency content (Bataller et al., 2019). In this method, three narrow frequency bins are split from the decomposed seismic data and assigned to the red (R), green (G), and blue (B) color channels, respectively (Bataller et al., 2019). Areas with similar frequency characteristics then appear in similar colors, allowing us to quickly spot patterns, transitions, or heterogeneities, such as intra-MTCs structures or fluid escape pipes (Eckersley et al., 2018).

3.3 MTCs and Gas hydrate observation

MTCs are bounded by a continuous high-amplitude basal shear surface and a rugose medium- to high-amplitude top surface (Moscardelli & Wood, 2008; Bull et al., 2009). MTCs are internally chaotic to transparent, contrasting sharply with the continuous, parallel reflections of the surrounding hemipelagic sediments (Moscardelli & Wood, 2008; Bull et al., 2009). From well log data, MTCs intervals are characterized by increased density, resistivity, and decreased porosity, permeability, compared to the overlying and underlying non-MTCs units (Dugan, 2012; Sawyer et al., 2009).

The presence of gas hydrates is identified through the presence of Bottom Simulating Reflector (BSR) in seismic data and the distinct petrophysical responses in the well log data. From seismic data, BSR is recognized as a high-amplitude reflection that parallels the seabed but has the opposite polarity to the seabed (Korenaga et al., 1997). It represents the acoustic impedance contrast between the hydrate-bearing sediments above and the free gas-bearing sediments below. From well log data, the hydrate-bearing intervals are defined by increased resistivity and P-wave velocity relative to the surrounding non-hydrate-bearing strata (Holbrook et al., 1996).

3.4 Permeability calculation

Permeability represents a direct quantitative indicator for evaluating seal potential (Schowalter, 1979). However, in situ measurements of permeability in fine-grained MTCs are difficult and costly to perform. To yield accurate permeability estimation for MTCs, we calculate the permeability from nuclear magnetic resonance measurements through empirical Schlumberger-Doll Research equation developed by Kenyon et al. (1988):

$$k = A\phi^4(T_{2LM})^2 \quad (1)$$

where φ $[m^3 \cdot m^{-3}]$ is the porosity, T_{2LM} $[ms]$ is the logarithmic mean of the T_2 distribution, and A $[m^2 \cdot m^{-2}]$ is the fitting coefficient.

The investigated MTCs here exhibit increased clay content, ranging from 20% to 50% (Liang et al., 2021; Kuang et al., 2023). For the determination of fitting coefficient A, we implement the function of lithology developed by Daigle and Dugan (2009) specifically for silt- and clay-rich sediments:

$$A = -2.7 \times 10^{-18} GR + 2.4 \times 10^{-16} \quad (2)$$

where GR $[gAPI]$ is the gamma ray log value.

While the empirical Schlumberger-Doll Research equation provides the feasible means of estimating permeability in fine-grained MTCs, we acknowledge that its accuracy is highly dependent on the fitting coefficient A (Kenyon et al., 1988). Although the lithology-dependent function developed by Daigle and Dugan (2009) can account for the high silt and clay content, this function is derived from general sedimentary environments and is not validated against core-measured permeability specific to the MTCs in the Qiongdongnan Basin. Therefore, the calculated permeability in our study should be treated as quantitative indicators for relative permeability variations, rather than absolute values of permeability.

3.5 Numerical modelling

To approximate the shear deformation within MTCs flowing above topographically variable strata, we implement a two-dimensional numerical solver based on implicit pseudo-transient methods and finite difference discretization (Räss et al., 2022; Liu et al., 2024). The momentum equations at steady state can be simplified to:

$$\frac{\partial \tau_{ij}}{\partial x_j} - \frac{\partial p}{\partial x_i} + F_i - \rho\left(u_j \frac{\partial u_i}{\partial x_j}\right) = 0 \tag{3}$$

where τ_{ij} $[Pa]$ is the deviatoric stress tensor, p $[Pa]$ is the isotropic pressure, $F_i = \rho g(sin\ \alpha, cos\ \alpha)$ $[kg \cdot s^{-2} \cdot m^{-2}]$ is the gravitational body force at a tilted angle α, $u_j \frac{\partial u_i}{\partial x_j}$ $[m \cdot s^{-2}]$ is the convective acceleration term, and $i \in \{x, z\}$ indexes the two spatial components.

Herein, we describe failing MTCs as mass flow with Herschel-Bulkley rheology behavior. Failing sediments behave as a fluid (i.e., $\tau > \tau_0$), thus neglecting the state of rigid solid. The rheology model for simple shear is implemented using:

$$\tau_{ij} = \tau_0 + k_0 \dot{\varepsilon}_{ij}^n \tag{4}$$

where τ_0 is the yield shear stress $[Pa]$, k_0 is the consistency index $[Pa \cdot s^n]$, n is the flow index $[dimensionless]$. The key physical parameters of modelled fluid can be found in Table 1.

Failing sediments flow into the domain from the left boundary above undeforming strata and exits at the right boundary. The analytical inflow field is calculated by solving the momentum balance along the flow at steady state. The outlet boundary condition is following the approach of Kreiss (1968), Gustafsson et al. (1972), and Orlanski (1976).

To prescribe the interface between MTCs and undeformed strata, we implement the immersed-boundary method, a fictitious domain method that allows us to treat fluid and solid domains separately and efficiently (Peskin, 1972, 2002). This method facilitates the independent and computationally

efficient handling of fluid and solid domains, making it well-suited for addressing the intricate geometries and dynamic interactions prevalent in MTCs (Peskin, 1972, 2002; Zhao et al., 2021).

The detailed explanations of numerical simulation considering pseudo-transient methods, rheology model generalization, boundary conditions, and immersed-boundary method can be accessed in **Appendix B**.

4 Results

4.1 MTC-1

Observation: MTC-1 is bounded by horizon H1 at its base and horizon H2 at its top (Figure 2). The lateral and distal boundaries of MTC-1 extend beyond the limits of the 3D seismic dataset. Structure map and variance attribute map from horizon H1 shows a series of E-trending lineations that are generally oriented downslope (Figure 3a & b). These lineations range from 50~100m in width, 2.5~5.0km in length, and exhibit erosional characteristics, cutting downward into the underlying substrate. The central region of MTC-1 contains a block-shaped feature and exhibits a higher-variance boundary compared to the surrounding area (Figures 3a & b). In the correlated seismic section, the block exhibits internally sub-parallel, continuous, high-amplitude seismic reflections (Figure 2). Below the block, the seismic reflections are marked by high-amplitude and negative polarity opposite to the seabed reflection (Figure 2). Within the blocks, pull-up reflections that vertically traverse the block and overlying MTC-1 (Figure 2). These pull-up seismic reflections form pipe like features extending to the seabed, where they generate 200~500m wide depressions on the seabed (Figure 2). The eastern region of MTC-1 shows a continuous SSW-trending scarp (Figure 3a). In the correlated seismic section, the scarp manifests as a segment of the basal shear surface that discordantly cuts up to a stratigraphically higher strata at a high angle (Figure 2). Spectral decomposition attribute extracted from horizon H1 shows a series of concave-eastward, regularly spaced subparallel lineations developed adjacent to the easternmost part of the scarp (Figure 3c). These subparallel lineations appear in seismic section as semicontinuous, medium-amplitude reflections (Figure 2).

Interpretation: The E-trending lineations are interpreted as grooves, forming by clasts entrained within the host flow that abraded the contemporaneous seabed (Figure 3d; Posamentier and Martinsen, 2011; Sobiesiak et al., 2018). Grooves typically develop parallel to the main flow direction, suggesting that MTC-1 was emplaced in a E-direction (Bull et al., 2009). The block-shaped feature, characterized by internally sub-parallel, continuous seismic reflections, is interpreted as a remnant block, representing an isolated segment of sediment that has not undergone failure (Bull et al., 2009).

The pull-up seismic reflections with pipe-like geometries are interpreted as manifestations of fluid escape structures (Wang et al., 2025). The seabed depressions are interpreted as pockmarks in previous studies and are indicative of recurrent cold seep activity (Ye et al., 2019; Ren et al., 2024; Wang et al., 2025). Considering the spatial correlation between fluid escape structures that crosscut MTC-1, we infer that seal failure has occurred at the location of the remnant block.

The SSW-trending scarp is interpreted as a frontal ramp, formed by the upward incision of the MTCs into shallower stratigraphic levels (Bull et al., 2009; Joanne et al., 2013). The concave-eastward, regularly spaced subparallel lineations are interpreted as pressure ridges, formed by a combination of shear compression and resistance from the undeformed sediments during the deceleration and eventual cessation of MTCs movement (Figure 3d; Bull et al., 2009; Joanne et al., 2013; Ortiz-Karpf et al., 2018).

4.2 MTCs 2&3

Observation: MTC-2 is bounded by Horizon H3 at its base and Horizon H4 at its top (Figure 2). Its lateral extent surpasses the limits of the available 3D seismic dataset. Variance and spectral decomposition attributes extracted from the basal shear surface (H3) reveal a series of E-trending lineations, morphologically comparable to those on Horizon H1 (Figures 4a–4c). These lineations terminate at the distal edge of MTC-2, defining a distinct boundary that marks the downslope limit of the MTC-2 (Figures 4b & 4c).

MTC-3 is confined between Horizon H5 at the base and Horizon H6 at the top (Figure 2). Its lateral

margin extends beyond the 3D seismic dataset. Variance and spectral decomposition attributes from Horizon H5 reveal a basal shear surface characterized by E-trending lineations, ranging from 0.1~2.5 km in width and 2.5~15 km in length (Figure 5a–5c). These E-trending lineations exhibit a divergent pattern downslope, suggesting flow spreading and possible lateral unconfined emplacement (Figure 5c). The termination of these grooves delineates the distal margin of MTC-3, marked by a distinct boundary of seismic striation cessation (Figures 5b & 5c).

A cluster of semi-rounded, crater-like depressions measuring 50~100 m in diameter is observed beyond the distal margins of MTC-2 and MTC-3 (Figures 4b & 5b). In the variance attribute map, they correspond to zones of increased variance (Figure 6a), while the spectral decomposition map shows scattered bright spots coinciding with their locations (Figure 6b). In seismic sections, the depressions are situated directly above the frontal ramp beneath MTC-1 (Figures 6c & 6d). They are bounded by near-vertical (~90°) discontinuities but lack internal deformation typically linked to MTCs emplacement, such as folding or faulting.

Interpretation: Consistent with MTC-1, the E-trending lineations on the basal shear surface of MTC-2 and MTC-3 are interpreted as grooves (Figure 4d & 5d; Posamentier and Martinsen, 2011; Sobiesiak et al., 2018). The E-trending erosional features with divergent shape on the basal shear surface of MTC-3 are interpreted as scours, formed when the basal drag is great enough to allow the mass movement to plough into the substrate (Figure 5d; Sobiesiak et al., 2018). Considering the kinematic indicators provided by grooves and scours, the emplacement direction of MTC-2 and MTC-3 is inferred as E-in general.

The semi-rounded, crater-like depressions observed beyond the distal margins of MTC-2 and MTC-3 suggest a post-emplacement origin, likely associated with vertical fluid escape (Figure 6d). Additionally, an exploration well drilled near the fluid escape pipes was halted due to significant influx of methane gas from the borehole, confirming the escaping fluids were methane-bearing (Kuang et al., 2023). The semi-rounded, crater-like depressions are thus interpreted as fluid escape

pipes caused by the seepage of methane-bearing fluids (Figure 6d; Cartwright & Santamarina, 2015; Ye et al., 2019). The presence of fluid escape pipes directly above the frontal ramp of MTC-1 (Figure 6d) suggests that seal failure occurred at the frontal ramp crest.

4.3 MTCs petrophysical properties

Observation: Compared to the surrounding non-MTCs units, MTCs are normally characterized by increased density (1.8~2.0 g/cm³), resistivity (1.3~2.5 Ω·m), and decreased porosity (45~65%), permeability (0.5~6.5 mD), which remains consistent with previously published studies (Figure 7; Dugan, 2012; Sawyer et al., 2009; Wu et al., 2022). However, the petrophysical properties of MTC-1change abruptly across the deposit, with intervals overlying remnant blocks and frontal ramps showing markedly different characteristics compared with the surrounding portions of the MTCs that lack such underlying structures. Intervals of MTC-1 that overlie the remnant block and frontal ramp display distinctly different petrophysical characteristics, including lower density (1.6~1.7 g/cm³), lower resistivity (0.7~1.6 Ω·m), and higher porosity (55~80%) and permeability (2.5~10.5 mD) compared to the normal MTC-1 intervals devoid of these features (Figure 8). More specifically, the density of MTC-1 intervals overlying the remnant block and frontal ramp is approximately 13% lower than that of remaining parts of MTC-1 (Figure 8a), while resistivity decreases by ~39% (Figure 8b), porosity increases by ~23% (Figure 8c), and permeability increases by ~217% (Figure 8d).

Interpretation: The significantly lower density and resistivity, coupled with higher porosity and permeability observed in MTC-1 intervals overlying the remnant block and frontal ramp, indicate a substantially reduced degree of compaction. The reduced compaction in MTC-1 intervals overlying the remnant block and frontal ramp implies that the seal potential in these zones is significantly weakened. This is consistent with the fluid escape structures observed above the remnant block and frontal ramp (Figure 2 & Figure 6). Thus, the seal potential of MTC-1 varies spatially, with intervals overlying the remnant block and frontal ramp showing lower degrees of compaction and consequently reduced seal potential.

5 Discussions and Implications

5.1 Shear localization as a key control on MTCs seal potential

Previous studies have identified two primary mechanisms responsible for MTCs seal failure: (1) fault-controlled fluid migration, where normal or thrust faults provide permeable pathways for fluid escape (e.g., Pattier et al., 2013; Yang et al., 2013); and (2) overpressure-driven breaching, where MTCs emplacement induces overpressure in underlying strata, triggering upward fluid migration and seal failure (e.g., Moernaut et al., 2017). In this study, the three MTCs exhibit no seismically resolvable internal faulting, and no evidence of overpressure is observed in the underlying gas hydrate system (Kuang et al., 2023), suggesting that neither fault-assisted nor overpressure-driven mechanisms can account for the observed seal failure. The following section investigates the potential triggers of MTCs seal failure in the study area.

We use a two-dimensional numerical solver based on finite difference discretization and implicit pseudo-transient methods to model the distribution and evolution of shear strain during MTCs emplacement (Räss et al., 2022; Trujillo-Vela et al., 2022). Numerical simulation shows that, under conditions of low-gradient (tilt angle 1.2°) basal shear surface without remnant block or frontal ramp, shear strain consistently develops within a 4.0~8.0, representing approximately 10~20% of the total MTCs thickness confined to its lowermost part (Figure 9a). This concentration of shear strain is referred to as shear localization, characterized by a distinct deformation band with increased shear strain rates during MTCs emplacement (Anders et al., 2000; Mitchell et al., 2015; Steventon et al., 2019). Shear localization describes the phenomenon where strain is not distributed uniformly and instead concentrates at a narrow band-like region. The boundary between the moving MTCs and the underlying in-situ strata is where the maximum velocity and rheology contrast locate (Anders et al., 2000; Mitchell et al., 2015; Steventon et al., 2019). Therefore, the shear localization normally occurs near the base of MTCs, forming the basal shear zone. The presence of shear localization in the lower part of the MTCs is consistent with petrophysical and outcrop-based studies, which identify the lowermost 15~30 m, accounting for 10~20% MTCs total thickness, as the densest interval that

accommodated the majority of shear deformation during emplacement (Hodgson et al., 2019; Wu et al., 2021).

As seismic and well log interpretations reveal that seal failure occurs in MTC-1 where it overlies the remnant block and frontal ramp, we simulate two additional emplacement scenarios. In the first scenario, when the MTC encounters a frontal ramp, shear strain intensifies along the ramp edge but diminishes across the ramp crest (Figure 9b). In the second scenario, when the MTC collides with a remnant block, shear strain similarly increases along the block margins but is markedly reduced across the block crest (Figure 9c). These modelling results, together with our seismic observations, indicate that the formation of the remnant block and frontal ramp is attributed to the gas hydrate or sandy turbidite in the in-situ strata predating MTC-1 emplacement (Figure 10a; Yang et al., 2013; Wan et al., 2022; Kuang et al., 2023). The strengthening effect of hydrates and sandy turbidites increased the shear strength of these strata by raising the critical shear stress threshold (Mitchener & Torfs, 1996; Madhusudhan et al., 2019). As a result, MTC-1 was unable to erode these mechanically strengthened strata and instead ramped up and over them, preserving them as remnant blocks or frontal ramps (Figure 10b).

When MTCs overrides such mechanically strengthened strata, shear localization weakens above the resulting remnant block or frontal ramp. The associated reduction in shear strain suppresses shear compaction in these intervals, thereby lowering their seal potential. This mechanism is fully consistent with the petrophysical evidence, in which MTC-1 intervals overlying the remnant block and frontal ramp exhibit lower density and resistivity, and higher porosity and permeability, reflecting reduced compaction. Seal failure in these zones may be further enhanced by locally thin MTCs cover and by fluid focusing around the remnant block (Gamboa et al., 2011).

MTCs seal potential is primarily controlled by shear localization, as shear strain plays a key role in shaping the microstructure of granular materials (Figure 11a). High shear strain promotes grain size reduction (Mitchell et al., 2015; Siman-Tov & Brodsky, 2018), collapse of pore bodies (Emmanuel

& Day-Stirrat, 2012; Cardona et al., 2016) and realignment of pore throats (Kanamatsu et al., 2014; Cardona et al., 2016; Roy et al., 2022). In contrast, low shear strain inhibits these processes and instead promotes partial elastic rebound, allowing pore structures to reopen and seepage pathways to widen (Gatter et al., 2021; Zhao et al., 2023). Thus, the low strain in MTCs intervals overlying the remnant block and frontal ramp lead to elastic rebound and limited grain size rearrangement, which together widen seepage pathways and increase permeability (Figure 11b). This reduction in shear compaction ultimately weakens the seal potential of these intervals and results in localized seal failure. In comparison, areas of normal topography, or the edges of strengthened in-situ strata, tend to experience increased shear strain during emplacement. These high-strain zones undergo grain size reduction, pore-throat collapse, and directional pore alignment (Figure 11c; Gatter et al., 2021). This increases compaction and enhances the seal potential of MTCs, thereby reducing the likelihood of seal failure in such regions.

5.2 Implications for gas hydrate formation and distribution

Previous studies indicate that the BSRs in our study area display complex fluid migration and re-accumulation behavior, as reflected by the presence of multiple double BSRs (Yang et al., 2013; Wan et al., 2022). In this section, we focus on the re-accumulated gas hydrates after the emplacement of MTC-3, rather than the residue gas hydrates responsible for generating the remnant block. Where MTC-1 remains highly compacted and preserves a well-developed basal shear zone (i.e., in areas lacking remnant blocks and frontal ramp), it retains high seal potential. This allows methane-rich fluids sourced the Songnan Low Uplift to accumulate beneath the MTCs, forming BSR 1 (Table 2; Figure 12; Kuang et al., 2023). The free gas associated with BSR 1 then migrates laterally, providing the methane necessary for the subsequent formation of BSR 2 and BSR 3 (Figure 12).

BSR 2 lies beneath an area where MTC-1 also retains high seal potential. Under such conditions, increased pressures favor gas-hydrate crystallization as methane-rich fluids cool during long-distance lateral advection (Sloan, 2003; Walsh et al., 2009; Crutchley et al., 2014). This process ultimately

leads to the formation of high-saturation gas hydrates in BSR 2 (Table 2; Figure 12). In contrast, upon reaching the crest of frontal ramp, where the seal potential of MTC-1 is compromised, methane-rich fluids are able to migrate vertically. This upward migration traverses the under-compacted zones in MTC-1 and the overlying MTC-2 and MTC-3, producing crater-like pockmarks on the seabed that record focused fluid escape (Figure 12).

In contrast, BSR 3 lies beneath an area where the MTC-1 interval overlies a remnant block and displays reduced seal potential (Figure 12). Under these weakened seal conditions, only moderate pressures develop, allowing methane-rich fluids to partially crystallize into gas hydrate during advective cooling while the remaining fraction persists as free gas (Ker et al., 2019; Milkov et al., 2004; Ruppel & Kessler, 2017). This results in low-saturation gas hydrates that coexist with free gas in BSR 3 (Table 2; Figure 12). The residual free gas then migrates upward through the under-compacted zones above the remnant block and ultimately breaches the seabed, forming a cluster of pockmarks and a cold seep system (Figure 12; Wang et al., 2025).

Thus, we demonstrate that the seal potential of MTCs is a first-order control on subsurface fluid migration and hydrate accumulation. Where MTCs remain highly compacted and preserve a continuous basal shear zone (i.e., lacking frontal ramps or remnant blocks), they function as effective seals that prevents the vertical migration of methane-rich fluids. This promotes the development of laterally focused free-gas accumulations (e.g., BSR 1) or high-saturation gas hydrates (e.g., BSR 2), depending on the prevailing pressure-temperature conditions. In contrast, where basal shear zones are disrupted by the presence of remnant blocks or frontal ramps, the seal potential of the MTCs is reduced. In these zones, free gas can migrate vertically, producing seabed pockmarks when gas supply is limited, or forming mixed-phase systems of coexisting free gas and low-saturation gas hydrates when gas supply is sustained (e.g., BSR 3). Therefore, spatial variations in the seal potential of MTCs dictate fluid migration pathways and exert a direct control on the formation, saturation, and distribution of gas hydrates.

6 Conclusions

In this study, we integrate 3D seismic reflection and well log data to investigate the sealing behavior of three vertically stacked MTCs in the Qiongdongnan Basin, northern South China Sea, with the aim of identifying the key factor that control their seal potential. We show that:

(1) Shear localization normally develops in the lowermost part of MTCs during emplacement, forming a narrow (10~20% MTCs total thickness), highly deformed basal shear zone. This shear deformation enhances MTCs compaction, reduces porosity and permeability, and is therefore critical for the seal potential of MTCs.

(2) The remnant block and frontal ramp can disrupt shear localization during MTCs emplacement. This disruption results in lower degrees of compaction and higher permeability in intervals of MTCs overlying these basal structures, ultimately leading to seal failure at these locations.

(3) The quality of MTCs seals plays a key role in the spatial distribution and accumulation of gas hydrates. MTCs with high seal potential promote the accumulation of free gas or high-saturation hydrates, whereas those with reduced seal potential lead to low-saturation hydrates coexisting with free gas.

(4) Understanding the conditions under which MTCs function as effective seals, or fail, is crucial for predicting gas hydrate distribution and identifying suitable sites for carbon sequestration in submarine settings. Therefore, such knowledge of subsurface fluid flow is critical for derisking future hydrocarbon exploration and carbon sequestration initiatives.

Appendix A: Seismic well tie

We show one example of seismic-well tie using W1 (Figure A2). Here, sonic and density logs are used to generate synthetic seismograms:

$$Reflection\ coefficient = \frac{\rho_2 v_2 - \rho_1 v_1}{\rho_2 v_2 + \rho_1 v_1} \quad \text{(A1)}$$

where ρ is density $[kg \cdot m^{-3}]$, v is P-wave velocity $[m \cdot s^{-1}]$, and the subscripts denote two subsurface layers.

The set of reflection coefficients is then band limited to the same frequency band as the actual seismic data (Lines & Newrick, 2004). Between the well log synthetic seismograms and actual seismic data, correlations are made through the vertical stretch or squeeze of the seismograms to match key subsurface intervals. Finally, the relationship between depth domain well log data and time domain seismic data can be established.

Appendix B: Numerical modelling

B1. Implicit pseudo-transient methods

The implicit pseudo-transient method is a powerful numerical technique renowned for its robustness in tackling highly nonlinear problems, such as shear band formation in visco-elasto-plastic media (Räss et al., 2022). This iterative approach enhances stability in the solution process by introducing a pseudo-time derivative, making it highly effective for modeling complex rheological behaviors (Räss et al., 2022). Studies have shown it can deliver over 96% parallel efficiency on distributed-memory systems utilizing up to 2197 graphics processing units (Räss et al., 2022). Under these circumstances, implicit pseudo-transient method possesses high robustness and scalability, which makes it well suited for solving the momentum equation to approximate the shear deformation within MTCs.

At each physical time step, implicit pseudo-transient method is implemented for the iterative solution to the momentum equation:

$$\frac{\partial p}{\partial \Gamma_p} = -\frac{\partial u_i}{\partial x_i} \tag{B1}$$

$$\frac{\partial u_i}{\partial \Gamma_u} = \frac{\partial \tau_{ij}}{\partial x_j} - \frac{\partial p}{\partial x_i} + F_i - \rho\left(u_j \frac{\partial u_i}{\partial x_j}\right) \tag{B2}$$

where Γ presents the pseudo-time step.

An implicit solution of the momentum equations can be achieved when the continuity residual $\frac{\partial p}{\partial \Gamma_p}$ and the momentum residual $\frac{\partial u_i}{\partial \Gamma_u}$ are minimized. The detailed implementation processes of implicit pseudo-transient methods can be found in Räss et al. (2022).

B2. Herschel-Bulkley rheology model

The generalized rheology model for simple shear is implemented using:

$$\tau_{ij} = \tau_0 + k_0 \dot{\varepsilon}_{ij}^n \tag{B3}$$

$$\left|\frac{\dot{\varepsilon}_{ij}}{\dot{\varepsilon}_r}\right|^n = \mathrm{sgn}\left(\dot{\varepsilon}_{ij}\right)\frac{\tau_{ij}}{\tau_0} - 1 \tag{B4}$$

where τ_0 is the yield shear stress $[Pa]$, k_0 is the consistency index $[Pa \cdot s^n]$, n is the flow index $[dimensionless]$, $\dot{\varepsilon}_{ij}$ is the strain rate tensor $[s^{-1}]$, given as:

$$\dot{\varepsilon}_{ij} = \sqrt{\frac{1}{2}\tau_{ij}\tau_{ij}} \tag{B5}$$

$\dot{\varepsilon}_r$ is the reference strain rate $[s^{-1}]$, given as:

$$\dot{\varepsilon}_r = \left(\frac{\tau_0}{k_0}\right)^{\frac{1}{n}} \tag{B6}$$

The detailed implementation processes can be found in Zafar et al. (2024).

B3. Outlet boundary conditions

We use the outlet boundary condition from Orlanski (1976). This boundary condition allows phenomena generated in the domain of interest to pass through the boundary without undergoing significant distortion or influencing the interior solution, and it is an optimal solution for balancing accuracy and efficiency.

$$\frac{\partial u}{\partial t} + U\frac{\partial u}{\partial x} = 0 \tag{B7}$$

From Kreiss (1968) and Gustafsson et al. (1972), the propagation speed U is numerically estimated by $U = \frac{\Delta x}{\Delta t}$, where Δx and Δt are the spatial and temporal grid sizes. The speed at the outlet boundary is then as follows:

$$u_{n_x}^{n_t} = 2u_{n_{x-1}}^{n_{t-1}} - u_{n_{x-2}}^{n_{t-2}} \tag{B8}$$

where n_x is the boundary point and n_t is the current time step.

B4. Immersed-boundary method

Immersed-boundary method is used to prescribe the fictitious interface between MTCs and undeformed strata. The general idea is using both Eulerian and Lagrangian approaches to solve the governing equations on the MTCs domain with a correction on the interface between MTCs and undeformed strata (Zhao et al., 2021). Lagrangian approach describes fluid motion focusing on an individual fluid parcel as it moves through space and time, while Eulerian approach describes fluid motion focusing on specific locations in the space through which the fluid flows as time passes (Peskin, 1972, 2002). The interface (the immersed boundary) is represented independently as a set of discrete points (Lagrangian variables) that define its shape and position (Peskin, 1972, 2002). This interface cuts through the MTCs domain grid (Eulerian variables), which is the fixed grid where the governing equations are solved (Peskin, 1972, 2002). This method avoids the computationally expensive and often challenging task of generating and deforming body-conforming meshes for intricate or rapidly moving boundaries (e.g. basal shear surface). The detailed implementation processes of the immersed-boundary method can be found in Zhao et al. (2021) and Liu et al. (2024).

Appendix C: Gas hydrate saturation estimation

To determine the actual formations of multiple amplitude anomalies in seismic data, gas hydrate saturation is calculated using Archie's porosity-resistivity equation and saturation equation (Archie,

491 1942):

492 $$S_h = 1 - \left(\frac{R_0}{R_m}\right)^{\frac{1}{n_{Ar}}}, \qquad R_0 = \frac{R_w}{\phi^m} \tag{C1}$$

493 where S_h $[m^3 \cdot ms^{-3}]$ is the gas hydrate saturation, R_0 $[\Omega_m]$ is the background resistivity, R_m $[\Omega_m]$
494 is the measured resistivity, n_{Arch} $[dimensionless]$ is Archie's saturation exponent (set equal to 2.5
495 according to Cook and Waite, 2018), R_w $[\Omega_m]$ is the pore water resistivity (set equal to $0.3\Omega_m$
496 according to the resistivity of seawater), m is the cementation exponent (set equal to 2 according to
497 Cook et al., 2023).

498 **Acknowledgments**

499 We thank the Editor-in-Chief, Prof. Atle Rotevatn for his handling of our manuscript. We thank Dr.
500 Harya Nugraha and Dr. Sebastian Cardona for their constructive reviews, which have significantly
501 improved the quality of this paper. We thank Dr. Biwen Wang and Prof. Guangfa Zhong for the
502 helpful discussion during the manuscript preparation. We thank the Guangzhou Marine Geological
503 Survey for providing seismic and well log data and for granting permission to publish this work. This
504 research is supported by the National Key Research and Development Program of China (Grant No.
505 2021YFC2800901). The corresponding author acknowledges financial support from the National
506 Natural Science Foundation of China (Grant No. 42406060), the Natural Science Foundation of
507 Shanghai (Grant No. 23ZR1467800), and the Fundamental Research Funds for the Central
508 Universities, China.

509 **Data Availability Statement**

510 The 3D seismic and well log data were obtained from a series of proprietary surveys conducted by
511 the Guangzhou Marine Geological Survey in 2018, 2021 and 2022 for the gas hydrate exploration.
512 These data, uploaded by Kuang et al. (2023), are available in the Zenodo repository
513 (https://doi.org/10.5281/zenodo.7721790). The codes used for numerical simulations are available in
514 the Zenodo repository (https://zenodo.org/records/16252096). Requests for datasets can be made

through Guangzhou Marine Geological Survey via the corresponding author.

References

Alves, T. M., & Cartwright, J. A. (2010). The effect of mass-transport deposits on the younger slope morphology, offshore Brazil. *Marine and Petroleum Geology*, *27*(9), 2027–2036. https://doi.org/10.1016/j.marpetgeo.2010.05.006

Alves, T. M., Kurtev, K., Moore, G. F., & Strasser, M. (2014). Assessing the internal character, reservoir potential, and seal competence of mass-transport deposits using seismic texture: A geophysical and petrophysical approach. *AAPG Bulletin*, *98*(4), 793–824. https://doi.org/10.1306/09121313117

Anders, M. H., Aharonov, E., & Walsh, J. J. (2000). Stratified granular media beneath large slide blocks: Implications for mode of emplacement. *Geology*, *28*(11), 971–974. https://doi.org/10.1130/0091-7613(2000)28<971:SGMBLS>2.0.CO;2

Anomneze, D. O., Oguadinma, V. O., Ayodele, I. J., & Ajaegwu, N. E. (2025). Application of iso-frequency extractions and spectral frequency blending in hydrocarbon delineation of thin-pay and thick-pay reservoirs, Niger Delta Basin. *Energy Geoscience*, *6*(2), 100396. https://doi.org/10.1016/j.engeos.2025.100396

Archie, G. E. (1942). The Electrical Resistivity Log as an Aid in Determining Some Reservoir Characteristics. *Transactions of the AIME*, *146*(01), 54–62. https://doi.org/10.2118/942054-G

Bataller, F. J., McDougall, N., & Moscariello, A. (2019). Ordovician glacial paleogeography: Integration of seismic spectral decomposition, well sedimentological data, and glacial modern analogs in the Murzuq Basin, Libya. *Interpretation*, *7*(2), T383–T408. https://doi.org/10.1190/INT-2018-0069.1

Bull, S., Cartwright, J., & Huuse, M. (2009). A review of kinematic indicators from mass-transport complexes using 3D seismic data. *Marine and Petroleum Geology*, 26(7), 1132–1151. https://doi.org/10.1016/j.marpetgeo.2008.09.011

Cardona, S., Kobayashi, H., Wood, L., Dugan, B., & Milkov, A. V. (2022). Assessing the sealing quality of submarine mass transport complexes and deposits. *Marine and Petroleum Geology*, 143, 105748. https://doi.org/10.1016/j.marpetgeo.2022.105748

Cardona, S., Wood, L.J., Day-Stirrat, R.J., Moscardelli, L. (2016). Fabric Development and Pore-Throat Reduction in a Mass-Transport Deposit in the Jubilee Gas Field, Eastern Gulf of Mexico: Consequences for the Sealing Capacity of MTDs. In: Lamarche, G., *et al.* Submarine Mass Movements and their Consequences. Advances in Natural and Technological Hazards Research, vol 41. Springer, Cham. https://doi.org/10.1007/978-3-319-20979-1_3

Cartwright, J., Huuse, M., & Aplin, A. (2007). Seal bypass systems. *AAPG bulletin*, *91*(8), 1141-1166.

Cartwright, J., & Santamarina, C. (2015). Seismic characteristics of fluid escape pipes in sedimentary basins: Implications for pipe genesis. *Marine and Petroleum Geology*, *65*, 126-140.

Chen, D., Zhang, G., Dong, D., Zhao, M., & Wang, X. (2022). Widespread Fluid Seepage Related to Buried Submarine Landslide Deposits in the Northwestern South China Sea. *Geophysical Research Letters*, *49*(6), e2021GL096584. https://doi.org/10.1029/2021GL096584

Chopra, S., & Marfurt, K. J. (2007). *Seismic Attributes for Prospect Identification and Reservoir Characterization*. Society of Exploration Geophysicists and European Association of Geoscientists and Engineers. https://doi.org/10.1190/1.9781560801900

Cook, A. E., Portnov, A., Heber, R. C., Vadakkepuliyambatta, S., & Bünz, S. (2023). Widespread subseafloor gas hydrate in the Barents Sea and Norwegian Margin. *Earth and Planetary Science Letters*, *604*, 117993. https://doi.org/10.1016/j.epsl.2023.117993

562 Cook, A. E., & Waite, W. F. (2018). Archie's Saturation Exponent for Natural Gas Hydrate in Coarse-
563 Grained Reservoirs. *Journal of Geophysical Research: Solid Earth*, *123*(3), 2069–2089.
564 https://doi.org/10.1002/2017JB015138
565 Cox, D. R., Huuse, M., Newton, A. M. W., Gannon, P., & Clayburn, J. (2020). Slip sliding away:
566 Enigma of large sandy blocks within a gas-bearing mass transport deposit, offshore
567 northwestern Greenland. *AAPG Bulletin*, *104*(5), 1011–1043.
568 https://doi.org/10.1306/10031919011
569 Crutchley, G. J., Klaeschen, D., Planert, L., Bialas, J., Berndt, C., Papenberg, C., Hensen, C.,
570 Hornbach, M. J., Krastel, S., & Brueckmann, W. (2014). The impact of fluid advection on gas
571 hydrate stability: Investigations at sites of methane seepage offshore Costa Rica. *Earth and*
572 *Planetary Science Letters*, 401, 95–109. https://doi.org/10.1016/j.epsl.2014.05.045
573 Daigle, H., & Dugan, B. (2009). Extending NMR data for permeability estimation in fine-grained
574 sediments. *Marine and Petroleum Geology, 26*(8), 1419–1427.
575 https://doi.org/10.1016/j.marpetgeo.2009.02.008
576 Day-Stirrat, R. J., Flemings, P. B., You, Y., & van der Pluijm, B. A. (2013). Modification of mudstone
577 fabric and pore structure as a result of slope failure: Ursa Basin, Gulf of Mexico. *Marine*
578 *Geology*, *341*, 58–67. https://doi.org/10.1016/j.margeo.2013.05.003
579 Dugan, B. (2012). Petrophysical and consolidation behavior of mass transport deposits from the
580 northern Gulf of Mexico, IODP Expedition 308. *Marine Geology, 315–318*, 98–107.
581 https://doi.org/10.1016/j.margeo.2012.05.001
582 Eckersley, A. J., Lowell, J., & Szafian, P. (2018). High-definition frequency decomposition.
583 *Geophysical Prospecting*, *66*(6), 1138–1143. https://doi.org/10.1111/1365-2478.12642
584 Emmanuel, S., & Day-Stirrat, R. J. (2012). A framework for quantifying size dependent deformation
585 of nano-scale pores in mudrocks. *Journal of Applied Geophysics*, *86*, 29–35.
586 https://doi.org/10.1016/j.jappgeo.2012.07.011
587 Gamboa, D., Alves, T., & Cartwright, J. (2011). Distribution and characterization of failed
588 (mega)blocks along salt ridges, southeast Brazil: Implications for vertical fluid flow on
589 continental margins. *Journal of Geophysical Research: Solid Earth*, *116*(B8).
590 https://doi.org/10.1029/2011JB008357
591 Gatter, R., Clare, M. A., Kuhlmann, J., & Huhn, K. (2021). Characterisation of weak layers, physical
592 controls on their global distribution and their role in submarine landslide formation. *Earth-*
593 *Science Reviews*, *223*, 103845. https://doi.org/10.1016/j.earscirev.2021.103845
594 Gustafsson, B., Kreiss, H.-O., & Sundström, A. (1972). Stability Theory of Difference
595 Approximations for Mixed Initial Boundary Value Problems. II. *Mathematics of Computation*,
596 *26*(119), 649–686. https://doi.org/10.2307/2005093
597 Han, Z. (2025). Shear localization as a key control on mass-transport complexes seal integrity:
598 insights from geophysical datasets [Dataset]. *Zenodo.* https://zenodo.org/records/16252096
599 Hodgson, D. M., Brooks, H. L., Ortiz-Karpf, A., Spychala, Y., Lee, D. R., & Jackson, C. A.-L. (2019).
600 Entrainment and abrasion of megaclasts during submarine landsliding and their impact on
601 flow behaviour. *Geological Society, London, Special Publications*, *477*(1), 223–240.
602 https://doi.org/10.1144/SP477.26
603 Holbrook, W. S., Hoskins, H., Wood, W. T., Stephen, R. A., & Lizarralde, D. (1996). Methane
604 Hydrate and Free Gas on the Blake Ridge from Vertical Seismic Profiling. *Science*, *273*(5283),
605 1840–1843. https://doi.org/10.1126/science.273.5283.1840
606 Huang, B., Tian, H., Li, X., Wang, Z., & Xiao, X. (2016). Geochemistry, origin and accumulation of
607 natural gases in the deepwater area of the Qiongdongnan Basin, South China Sea. *Marine and*
608 *Petroleum Geology*, *72*, 254–267. https://doi.org/10.1016/j.marpetgeo.2016.02.007
609 Iverson, R. M. (1997). The physics of debris flows. *Reviews of Geophysics, 35*(3), 245–296.
610 https://doi.org/10.1029/97RG00426
611 Jackson, C. A.-L. (2011). Three-dimensional seismic analysis of megaclast deformation within a mass
612 transport deposit; implications for debris flow kinematics. *Geology*, *39*(3), 203–206.
613 https://doi.org/10.1130/G31767.1

Joanne, C., Lamarche, G., & Collot, J.-Y. (2013). Dynamics of giant mass transport in deep submarine environments: The Matakaoa Debris Flow, New Zealand. *Basin Research*, *25*(4), 471–488. https://doi.org/10.1111/bre.12006

Kaldi, J. G., & Atkinson, C. D. (1997). Evaluating seal potential: example from the Talang Akar Formation, offshore northwest Java, Indonesia.

Kanamatsu, T., Kawamura, K., Strasser, M., Novak, B., & Kitamura, Y. (2014). Flow dynamics of Nankai Trough submarine landslide inferred from internal deformation using magnetic fabric. *Geochemistry, Geophysics, Geosystems*, *15*(10), 4079–4092. https://doi.org/10.1002/2014GC005409

Karstens, J., Haflidason, H., Berndt, C., & Crutchley, G. J. (2023). Revised Storegga Slide reconstruction reveals two major submarine landslides 12,000 years apart. *Communications Earth & Environment*, *4*(1), 1–9. https://doi.org/10.1038/s43247-023-00710-y

Kenyon, W. E., Day, P. I., Straley, C., & Willemsen, J. F. (1988). A three-part study of NMR longitudinal relaxation properties of water-saturated sandstones. *SPE formation evaluation, 3*(03), 622-636.

Ker, S., Thomas, Y., Riboulot, V., Sultan, N., Bernard, C., Scalabrin, C., Ion, G., & Marsset, B. (2019). Anomalously Deep BSR Related to a Transient State of the Gas Hydrate System in the Western Black Sea. *Geochemistry, Geophysics, Geosystems*, *20*(1), 442–459. https://doi.org/10.1029/2018GC007861

Korenaga, J., Holbrook, W. S., Singh, S. C., & Minshull, T. A. (1997). Natural gas hydrates on the southeast U.S. margin: Constraints from full waveform and travel time inversions of wide-angle seismic data. *Journal of Geophysical Research: Solid Earth*, *102*(B7), 15345–15365. https://doi.org/10.1029/97JB00725

Kreiss, H.-O. (1968). Stability Theory for Difference Approximations of Mixed Initial Boundary Value Problems. I. *Mathematics of Computation*, *22*(104), 703–714. https://doi.org/10.2307/2004572

Kuang, Z., Cook, A., Ren, J., Deng, W., Cao, Y., & Cai, H. (2023). A Flat-Lying Transitional Free Gas to Gas Hydrate System in a Sand Layer in the Qiongdongnan Basin of the South China Sea. *Geophysical Research Letters, 50*(24), e2023GL105744. https://doi.org/10.1029/2023GL105744

Kuang, Z., Cook, A., Ren, J., Deng, W., Cao, Y., & Cai, H. (2023). A flat-lying transitional free gas to gas hydrate system in a sand layer in the Qiongdongnan Basin of the South China Sea [Dataset]. *Zenodo.* https://doi.org/10.5281/zenodo.7721790

Lastras, G., Canals, M., Urgeles, R., Hughes-Clarke, J. E., & Acosta, J. (2004). Shallow slides and pockmark swarms in the Eivissa Channel, western Mediterranean Sea. *Sedimentology*, *51*(4), 837-850.

Lenz, B. L., & Sawyer, D. E. (2022). Mass transport deposits in reflection seismic data offshore Oregon, USA. *Basin Research*, *34*(1), 81–98. https://doi.org/10.1111/bre.12611

Liang, C., Liu, C., Xie, X., Yu, X., He, Y., Su, M., Chen, H., Zhou, Z., Tian, D., Mi, H., Li, M., & Zhang, H. (2021). Basal shear zones of recurrent mass transport deposits serve as potential reservoirs for gas hydrates in the Central Canyon area, South China Sea. *Marine Geology*, *441*, 106631. https://doi.org/10.1016/j.margeo.2021.106631

Lines, L. R., & Newrick, R. T. (2004). *Fundamentals of geophysical interpretation*. Society of Exploration Geophysicists.

Liu, E. W., Räss, L., Herman, F., Podladchikov, Y., & Suckale, J. (2024). Spontaneous Formation of an Internal Shear Band in Ice Flowing Over Topographically Variable Bedrock. *Journal of Geophysical Research: Earth Surface, 129*(4), e2022JF007040. https://doi.org/10.1029/2022JF007040

Madhusudhan, B. N., Clayton, C. R. I., & Priest, J. A. (2019). The Effects of Hydrate on the Strength and Stiffness of Some Sands. *Journal of Geophysical Research: Solid Earth*, *124*(1), 65–75. https://doi.org/10.1029/2018JB015880

Milkov, A. V., Dickens, G. R., Claypool, G. E., Lee, Y.-J., Borowski, W. S., Torres, M. E., Xu, W., Tomaru, H., Tréhu, A. M., & Schultheiss, P. (2004). Co-existence of gas hydrate, free gas, and brine within the regional gas hydrate stability zone at Hydrate Ridge (Oregon margin): Evidence from prolonged degassing of a pressurized core. *Earth and Planetary Science Letters, 222*(3), 829–843. https://doi.org/10.1016/j.epsl.2004.03.028

Mitchell, T. M., Smith, S. A. F., Anders, M. H., Di Toro, G., Nielsen, S., Cavallo, A., & Beard, A. D. (2015). Catastrophic emplacement of giant landslides aided by thermal decomposition: Heart Mountain, Wyoming. *Earth and Planetary Science Letters*, *411*, 199–207. https://doi.org/10.1016/j.epsl.2014.10.051

Mitchener, H., & Torfs, H. (1996). Erosion of mud/sand mixtures. *Coastal Engineering*, *29*(1), 1–25. https://doi.org/10.1016/S0378-3839(96)00002-6

Moernaut, J., Wiemer, G., Reusch, A., Stark, N., De Batist, M., Urrutia, R., Ladrón de Guevara, B., Kopf, A., & Strasser, M. (2017). The influence of overpressure and focused fluid flow on subaquatic slope stability in a formerly glaciated basin: Lake Villarrica (South-Central Chile). *Marine Geology*, *383*, 35–54. https://doi.org/10.1016/j.margeo.2016.11.012

Moscardelli, L., & Wood, L. (2008). New classification system for mass transport complexes in offshore Trinidad. *Basin Research*, *20*(1), 73–98. https://doi.org/10.1111/j.1365-2117.2007.00340.x

Mountjoy, J. J., Pecher, I., Henrys, S., Crutchley, G., Barnes, P. M., & Plaza-Faverola, A. (2014). Shallow methane hydrate system controls ongoing, downslope sediment transport in a low-velocity active submarine landslide complex, Hikurangi Margin, New Zealand. *Geochemistry, Geophysics, Geosystems, 15*(11), 4137–4156. https://doi.org/10.1002/2014GC005379

Noda, A., TuZino, T., Joshima, M., & Goto, S. (2013). Mass transport-dominated sedimentation in a foreland basin, the Hidaka Trough, northern Japan. *Geochemistry, Geophysics, Geosystems*, *14*(8), 2638–2660. https://doi.org/10.1002/ggge.20169

Nugraha, H. D., Jackson, C. A.-L., Johnson, H. D., & Hodgson, D. M. (2020). Lateral variability in strain along the toewall of a mass transport deposit: A case study from the Makassar Strait, offshore Indonesia. *Journal of the Geological Society*, *177*(6), 1261–1279. https://doi.org/10.1144/jgs2020-071

Omosanya, K. O. (2018). Episodic fluid flow as a trigger for Miocene-Pliocene slope instability on the Utgard High, Norwegian Sea. *Basin Research*, *30*(5), 942–964. https://doi.org/10.1111/bre.12288

Orlanski, I. (1976). A simple boundary condition for unbounded hyperbolic flows. *Journal of computational physics*, *21*(3), 251-269.

Ortiz-Karpf, A., Hodgson, D. M., Jackson, C. A.-L., & McCaffrey, William. D. (2017). Influence of Seabed Morphology and Substrate Composition On Mass-Transport Flow Processes and Pathways: Insights From the Magdalena Fan, Offshore Colombia. *Journal of Sedimentary Research*, *87*(3), 189–209. https://doi.org/10.2110/jsr.2017.10

Ortiz-Karpf, A., Hodgson, D. M., Jackson, C. A.-L., & McCaffrey, W. D. (2018). Mass-transport complexes as markers of deep-water fold-and-thrust belt evolution: Insights from the southern Magdalena fan, offshore Colombia. *Basin Research*, *30*(S1), 65–88. https://doi.org/10.1111/bre.12208

Pattier, F., Loncke, L., Gaullier, V., Basile, C., Maillard, A., Imbert, P., Roest, W. R., Vendeville, B. C., Patriat, M., & Loubrieu, B. (2013). Mass-transport deposits and fluid venting in a transform margin setting, the eastern Demerara Plateau (French Guiana). *Marine and Petroleum Geology*, *46*, 287–303. https://doi.org/10.1016/j.marpetgeo.2013.06.010

Peskin, C. S. (1972). Flow patterns around heart valves: a numerical method. *Journal of computational physics*, *10*(2), 252-271.

Peskin, C. S. (2002). The immersed boundary method. *Acta numerica*, *11*, 479-517.

Posamentier, H. W., & Martinsen, O. J. (2011). The character and genesis of submarine mass-transport deposits: insights from outcrop and 3D seismic data. Mass-transport deposits in deepwater settings. *Society for Sedimentary Geology (SEPM) Special Publication, 96*, 7-38.

Räss, L., Utkin, I., Duretz, T., Omlin, S., & Podladchikov, Y. Y. (2022). Assessing the robustness and scalability of the accelerated pseudo-transient method. *Geoscientific Model Development*, *15*(14), 5757–5786. https://doi.org/10.5194/gmd-15-5757-2022

Ren, J., Qiu, H., Kuang, Z., Li, T., He, Y., Xu, M., Wang, X., Lai, H., & Liang, J. (2024). Deep-large faults controlling on the distribution of the venting gas hydrate system in the middle of the Qiongdongnan Basin, South China Sea. *China Geology, 7*(1), 36–50. https://doi.org/10.31035/cg2023086

Richardson, S. E. J., Davies, R. J., Allen, M. B., & Grant, S. F. (2011). Structure and evolution of mass transport deposits in the South Caspian Basin, Azerbaijan. *Basin Research*, *23*(6), 702–719. https://doi.org/10.1111/j.1365-2117.2011.00508.x

Roy, N., Frost, J. D., & Viggiani, G. (2022). Pore space evolution of granular assemblies under shear: An experimental study using X-ray tomography. *Granular Matter, 24*(2), 63.

Ruppel, C. D., & Kessler, J. D. (2017). The interaction of climate change and methane hydrates. *Reviews of Geophysics, 55*(1), 126–168. https://doi.org/10.1002/2016RG000534

Sawyer, D. E., Flemings, P. B., Dugan, B., & Germaine, J. T. (2009). Retrogressive failures recorded in mass transport deposits in the Ursa Basin, Northern Gulf of Mexico. *Journal of Geophysical Research: Solid Earth*, *114*(B10). https://doi.org/10.1029/2008JB006159

Schowalter, T. T. (1979). Mechanics of secondary hydrocarbon migration and entrapment. *AAPG bulletin*, *63*(5), 723-760.

Serov, P., Mattingsdal, R., Winsborrow, M., Patton, H., & Andreassen, K. (2023). Widespread natural methane and oil leakage from sub-marine Arctic reservoirs. *Nature Communications*, *14*(1), 1782. https://doi.org/10.1038/s41467-023-37514-9

Siman-Tov, S., & Brodsky, E. E. (2018). Gravity-Independent Grain Size Segregation in Experimental Granular Shear Flows as a Mechanism of Layer Formation. *Geophysical Research Letters, 45*(16), 8136–8144. https://doi.org/10.1029/2018GL078486

Sloan, E. D. (2003). Fundamental principles and applications of natural gas hydrates. *Nature*, 426(6964), 353–359. https://doi.org/10.1038/nature02135

Sobiesiak, M. S., Kneller, B., Alsop, G. I., & Milana, J. P. (2018). Styles of basal interaction beneath mass transport deposits. *Marine and Petroleum Geology, 98*, 629–639. https://doi.org/10.1016/j.marpetgeo.2018.08.028

Steventon, M. J., Jackson, C. A.-L., Hodgson, D. M., & Johnson, H. D. (2019). Strain analysis of a seismically imaged mass-transport complex, offshore Uruguay. *Basin Research*, *31*(3), 600–620. https://doi.org/10.1111/bre.12337

Su, M., Wu, C., Chen, H., Li, D., Jiang, T., Xie, X., Jiao, H., Wang, Z., & Sun, X. (2019). Late Miocene provenance evolution at the head of Central Canyon in the Qiongdongnan Basin, Northern South China Sea. *Marine and Petroleum Geology*, *110*, 787–796. https://doi.org/10.1016/j.marpetgeo.2019.07.053

Talling, P. J., Wynn, R. B., Masson, D. G., Frenz, M., Cronin, B. T., Schiebel, R., Akhmetzhanov, A. M., Dallmeier-Tiessen, S., Benetti, S., Weaver, P. P. E., Georgiopoulou, A., Zühlsdorff, C., & Amy, L. A. (2007). Onset of submarine debris flow deposition far from original giant landslide. *Nature, 450*(7169), 541–544. https://doi.org/10.1038/nature06313

Trujillo-Vela, M. G., Ramos-Cañón, A. M., Escobar-Vargas, J. A., & Galindo-Torres, S. A. (2022). An overview of debris-flow mathematical modelling. *Earth-Science Reviews*, *232*, 104135. https://doi.org/10.1016/j.earscirev.2022.104135

Walsh, M. R., Koh, C. A., Sloan, E. D., Sum, A. K., & Wu, D. T. (2009). Microsecond Simulations of Spontaneous Methane Hydrate Nucleation and Growth. *Science, 326*(5956), 1095–1098. https://doi.org/10.1126/science.1174010

Walton, M. A. L., Conrad, J. E., Papesh, A. G., Brothers, D. S., Kluesner, J. W., McGann, M., & Dartnell, P. (2024). A Comprehensive Assessment of Submarine Landslides and Mass Wasting Processes Offshore Southern California. *Geochemistry, Geophysics, Geosystems*, *25*(3), e2023GC011258. https://doi.org/10.1029/2023GC011258

768 Wan, Z.-F., Zhang, W., Ma, C., Liang, J.-Q., Li, A., Meng, D.-J., Huang, W., Yang, C.-Z., Zhang, J.-
769 F., & Sun, Y.-F. (2022). Dissociation of gas hydrates by hydrocarbon migration and
770 accumulation-derived slope failures: An example from the South China Sea. *Geoscience*
771 *Frontiers*, *13*(2), 101345. https://doi.org/10.1016/j.gsf.2021.101345
772 Wang, X., Wang, W., Jin, J., Zhang, G., Luan, Z., Li, C., Wang, M., Zhang, Z., Liu, B., Li, W., & Li,
773 S. (2025). Multiple observations to delineate the characteristics of cold seep system in the
774 Qiongdongnan Basin. *Marine and Petroleum Geology*, *181*, 107522.
775 https://doi.org/10.1016/j.marpetgeo.2025.107522
776 Wang, Y., Wang, Y., & Zhang, J. (2020). Connecting shear localization with the long-range
777 correlated polarized stress fields in granular materials. *Nature Communications*, *11*(1), 4349.
778 https://doi.org/10.1038/s41467-020-18217-x
779 Wu, N., Jackson, C. A.-L., Clare, M. A., Hodgson, D. M., Nugraha, H. D., Steventon, M. J., & Zhong,
780 G. (2022). Diagenetic priming of submarine landslides in ooze-rich substrates. Geology, 51(1),
781 85–90. https://doi.org/10.1130/G50458.1
782 Wu, N., Jackson, C. A.-L., Hodgson, D., Nugraha, H. D., & Zhong, F. G. (2024). Interactions between
783 buried mass-transport complexes and subsequent slope failures on a passive margin.
784 https://doi.org/10.31223/X5CT37
785 Wu, N., Jackson, C. A.-L., Johnson, H. D., & Hodgson, D. M. (2021). Lithological, petrophysical,
786 and seal properties of mass-transport complexes, northern Gulf of Mexico. *AAPG Bulletin,*
787 *105*(7), 1461–1489. https://doi.org/10.1306/06242019056
788 Wu, N., Jackson, C. A.-L., Johnson, H. D., Hodgson, D. M., & Nugraha, H. D. (2020). Mass-
789 transport complexes (MTCs) document subsidence patterns in a northern Gulf of Mexico
790 salt minibasin. *Basin Research*, *32*(6), 1300–1327. https://doi.org/10.1111/bre.12429
791 Yang, G., Yin, H., Gan, J., Wang, W., Zhu, J., Jia, D., Xiong, X., & Xu, W. (2022). Explaining
792 structural difference between the eastern and western zones of the Qiongdongnan Basin,
793 northern South China Sea: Insights from scaled physical models. *Tectonics*, *41*(2),
794 e2021TC006899.
795 Yang, J., Davies, R. J., & Huuse, M. (2013). Gas migration below gas hydrates controlled by mass
796 transport complexes, offshore Mauritania. *Marine and Petroleum Geology, 48*, 366–378.
797 https://doi.org/10.1016/j.marpetgeo.2013.09.003
798 Ye, J., Wei, J., Liang, J., Lu, J., Lu, H., & Zhang, W. (2019). Complex gas hydrate system in a gas
799 chimney, South China Sea. *Marine and Petroleum Geology*, *104*, 29–39.
800 https://doi.org/10.1016/j.marpetgeo.2019.03.023
801 Yoneda, J., Masui, A., Konno, Y., Jin, Y., Egawa, K., Kida, M., Ito, T., Nagao, J., & Tenma, N.
802 (2015). Mechanical properties of hydrate-bearing turbidite reservoir in the first gas production
803 test site of the Eastern Nankai Trough. *Marine and Petroleum Geology*, *66*, 471–486.
804 https://doi.org/10.1016/j.marpetgeo.2015.02.029
805 Zafar, M. N., Dutykh, D., Sabatier, P., Banjan, M., & Kim, J. (2024). Numerical Reconstruction of
806 Landslide Paleotsunami Using Geological Records in Alpine Lake Aiguebelette. *Journal of*
807 *Geophysical Research: Solid Earth*, *129*(5), e2023JB028629.
808 https://doi.org/10.1029/2023JB028629
809 Zhao, E., Dong, Y., Tang, Y., & Cui, L. (2021). Numerical study on hydrodynamic load and vibration
810 of pipeline exerted by submarine debris flow. *Ocean Engineering*, *239*, 109754.
811 https://doi.org/10.1016/j.oceaneng.2021.109754
812 Zhao, Y., Liu, J., Sang, S., Hua, L., Kong, L., Zeng, Z., & Yuan, Q. (2023). Experimental
813 investigation on the permeability characteristics of methane hydrate-bearing clayey-silty
814 sediments considering various factors. *Energy, 269*, 126811.
815 https://doi.org/10.1016/j.energy.2023.126811

816 **Table and Figure Captions**

817 Table 1. Parameters and corresponding values for numerical simulation.

818 Table 2. Petrophysical properties of BSRs and associated interpretations. Data are collected from the
819 raw well log data in W 1 to W 4. The values are shown as mean values of each parameter.

820 Figure 1. (a) Overview map of the South China Sea showing the boundary of the Qiongdongnan Basin
821 (red polygon). The black box indicates the extent of Figure 1b. The arrows indicate the sediment
822 transport directions. (b) Structural units of the Qiongdongnan Basin with locations of the 3D seismic
823 surveys and key wells. QDNB: Qiongdongnan Basin; SNLU: Songnan Low Uplift. LS18-1, LS18-2
824 and Y8-1 are adjacent conventional gas fields.

825 Figure 2. Perspective view of seismic volume with cross-wells section A-A' (See Figure 1b for
826 location). The upper surface of the seismic volume is shown as a horizon slice 25ms downwards from
827 seismic horizon H1.

828 Figure 3. (a) Structure map of Horizon H1 illustrating the basal shear surface of MTC-1. (b) Variance
829 attribute extracted along Horizon H1, showing the grooves, remnant block, frontal ramp. (c) Spectral
830 decomposition and associated frequency attribute extracted along Horizon H1, showing the pressure
831 ridges. RGB Blending is applied as 45Hz, 50Hz, and 60Hz. (d) Interpreted sketch of MTC-1, showing
832 its key kinematic indicators and transport direction.

833 Figure 4. (a) Structure map of Horizon H3 illustrating the basal shear surface of MTC-2. (b) Variance
834 attribute extracted along the surface 10ms above Horizon H3, showing the grooves, fluid escape pipes,
835 and boundaries of the MTC-2. (c) Spectral decomposition and associated frequency attributes
836 extracted along Horizon H3, showing the grooves, and boundaries of MTC-2. RGB Blending is
837 applied as 40Hz, 50Hz, and 60Hz. (d) Interpreted sketch of MTC-2, showing its boundaries, key
838 kinematic indicators, and transport direction.

839 Figure 5. (a) Structure map of Horizon H5 illustrating the basal shear surface of MTC-3. (b) Variance

840 attribute extracted along the surface 25ms above Horizon H5, showing the grooves, scours, fluid
841 escape pipes, and boundaries of MTC-3. (c) Spectral decomposition and associated frequency
842 attributes extracted along Horizon H5, showing the scours and boundaries of MTC-3. RGB Blending
843 is applied as 45Hz, 50Hz, and 60Hz. (d) Interpreted sketch of MTC-3, showing its boundaries, key
844 kinematic indicators, and transport direction.

845 Figure 6. (a) Variance horizon slice through the area with semi-rounded, crater-like depressions
846 (25ms above Horizon H5). See Figure 5d for the extent of Figure 6a. (b) Spectral decomposition
847 horizon slice through the area with semi-rounded, crater-like depressions (25ms above Horizon H5).
848 See Figure 5d for the extent of Figure 6b. (c) Uninterpreted seismic section B-B' showing the seismic
849 characteristics of semi-rounded, crater-like depressions. (d) Interpreted sketch of section B-B',
850 showing the high-angle deformation characteristics indicative of fluid escape pipes.

851 Figure 7. Multi-well correlation showing the log responses of MTCs, free gas-bearing sediments, and
852 gas hydrate-bearing sediments. The shaded blue units represent MTCs intervals. The shaded orange
853 units represent remnant block or frontal ramp intervals. GR: gamma ray; TNPH: thermal neutron
854 porosity; DEN: bulk density; RES_BS: shallow button resistivity; RES_BD: deep button resistivity;
855 *Vp*: P-wave velocity; Gas Vol: undisturbed zone gas volume fraction; DHAT: downhole annulus
856 temperature. See **Appendix C** for details of hydrate saturation calculations.

857 Figure 8. Petrophysical differences between MTC-1 intervals overlying the remnant block and frontal
858 ramp and other MTC-1 intervals. (a) density; (b) resistivity; (c) porosity; (d) permeability. The data
859 are retrieved from well log data in the interval between horizon H1 and H2, see Figure 2 and Figure
860 7 for more details. The depth of color reflects the kernel density which is a measurement of data
861 tendency.

862 Figure 9. Numerical simulation showing shear strain distribution in MTCs under different
863 topographies: (a) normal topography; (b) frontal ramp; (c) remnant block.

Figure 10. The formation process of the remnant block and frontal ramp. (a) MTC-1 pre-emplacement: Gas hydrate or sandy turbidites formed in the in-situ strata; (b) MTC-1 emplacement: MTC-1 was unable to erode strengthened in-situ strata, thus moving upward to avoid them; (c) MTC-1 post-emplacement: strengthened in-situ strata remained and manifested as remnant block or frontal ramp, depending on the extent of the strengthened intervals.

Figure 11. The role of shear localization in controlling seal potential of MTCs. (a) Three-dimensional sketch showing the effect of the strengthened in-situ strata on shear localization development; (b) microscopic change of pore structure when shear is weakened; (c) microscopic change of pore structure when shear is strengthened.

Figure 12. Three-dimensional schematic diagram showing the methane-bearing fluid migration pathways. Reddish yellow arrows indicate the migration of methane-bearing fluid. The upper surface of the seismic volume is a composite of two time slices at 2,490 ms and 2,536 ms in TWT to manifest three BSRs. Horizon slices of H1, H3, and H5 are presented to show the basal shear surfaces of MTCs. The locations of pockmarks are conceptual representations based on Figure 4 and Figure 5. BD: background deposit.

Figure A1. Demonstration of seismic-well tie using well W1 as an example.

Parameters	Notation	Unit	Value
Length of slope	L	m	4,800
Slope angle	α	$degree$	1.2
Density	ρ	$Kg \cdot m^{-3}$	1,700
Gravity acceleration	g	$m \cdot s^{-2}$	9.81
Yield stress	τ_0	Pa	8,000
Reference strain rate	$\dot{\varepsilon}_r$	s^{-1}	0.1
Flow index	n	/	0.75
Numerical grid resolution	n_x	/	511
	n_y	/	127
CFL coefficient	CFL	/	0.2

Table 1

Amplitude anomaly	Petrophysical properties				Interpretation
	Density	Resistivity	P-velocity	Temperature	
BSR 1	Low ~1.6 g/cm^3	Slightly high ~2 Ωm	Low ~1,600 m/s	High ~8 ^oC	Free gas sourced from the Songnan Low Uplift
BSR 2	Slightly high ~1.85 g/cm^3	High ~200 Ωm	High ~2,300 m/s	Low ~2 ^oC	High-saturation gas hydrate (~90% saturation)
BSR 3	Moderate ~1.8 g/cm^3	Slightly high ~2 Ωm	Slightly low ~1,700 m/s	High ~9 ^oC	Coexistence of free gas and low-saturation gas hydrate (~10% saturation)

Table 2

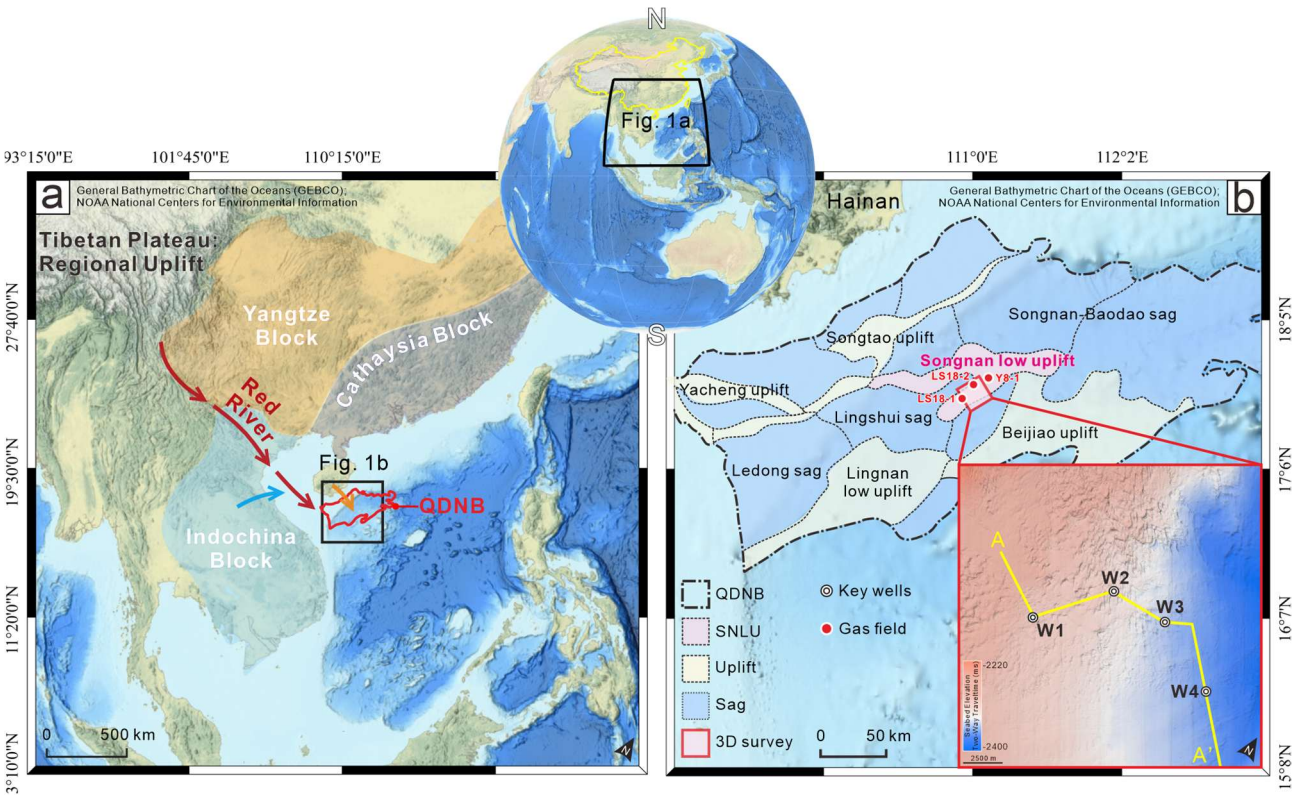
N
S
Fig. 1a
93°15'0"E
101°45'0"E
110°15'0"E
111°0'E
112°2'E
27°40'0"N
19°30'0"N
11°20'0"N
3°10'0"N
18°5'N
17°6'N
16°7'N
15°8'N
a
General Bathymetric Chart of the Oceans (GEBCO); NOAA National Centers for Environmental Information
Tibetan Plateau: Regional Uplift
Yangtze Block
Cathaysia Block
Red River
Fig. 1b
QDNB
Indochina Block
0
500 km
b
Hainan
Songnan-Baodao sag
Songtao uplift
Songnan low uplift
LS18-2
Y8-1
LS18-1
Yacheng uplift
Lingshui sag
Beijiao uplift
Ledong sag
Lingnan low uplift
QDNB
SNLU
Uplift
Sag
3D survey
Key wells
Gas field
0
50 km
A
A'
W1
W2
W3
W4
-2220
-2400
2500 m

Figure 1

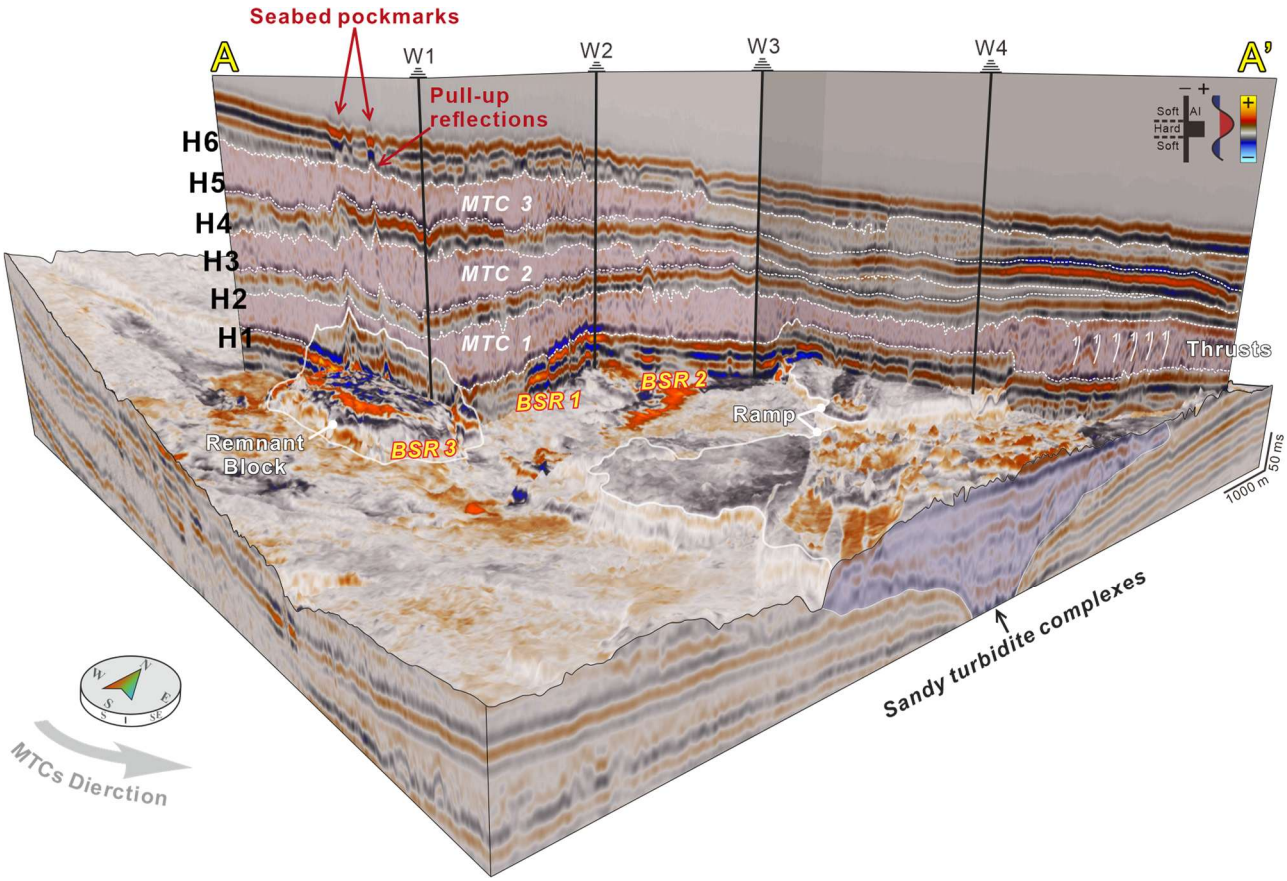

884

885 Figure 2

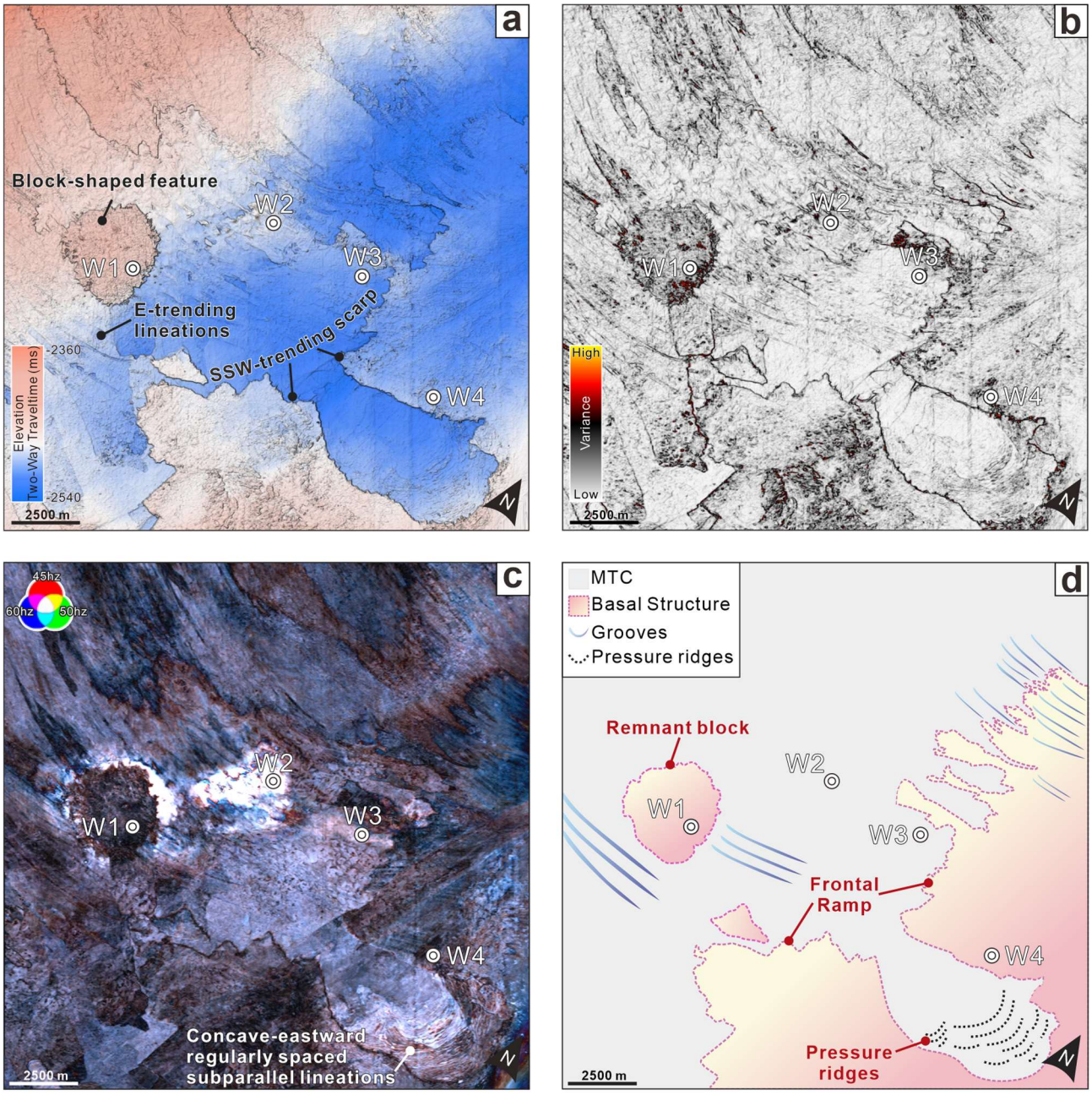

886

887 Figure 3

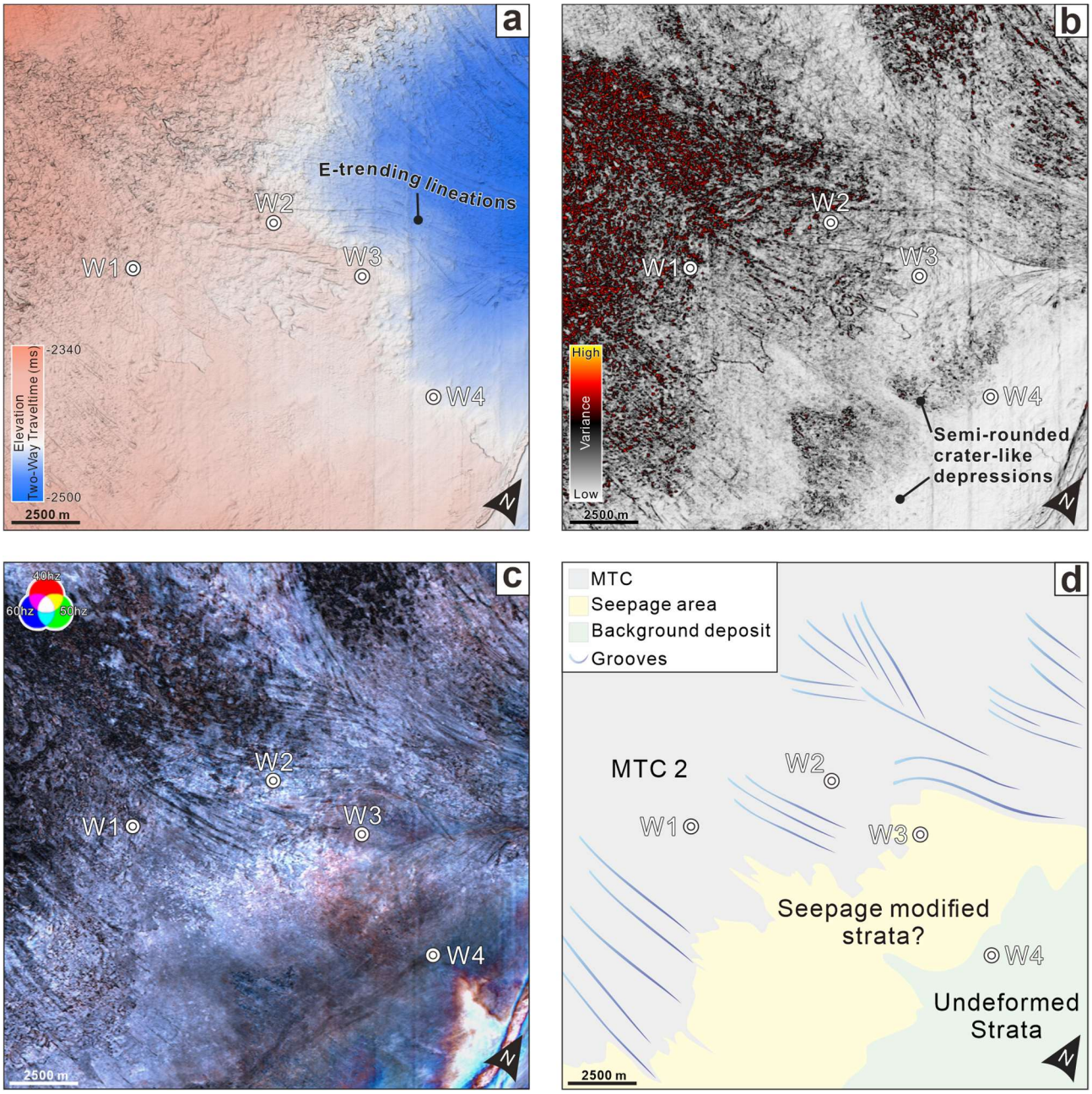
a
E-trending lineations
W1
W2
W3
W4
Elevation Two-Way Traveltime (ms)
-2340
-2500
2500 m
b
W1
W2
W3
W4
High
Variance
Low
Semi-rounded crater-like depressions
2500 m
c
40hz
60hz
50hz
W1
W2
W3
W4
2500 m
d
MTC
Seepage area
Background deposit
Grooves
MTC 2
W1
W2
W3
W4
Seepage modified strata?
Undeformed Strata
2500 m

Figure 4

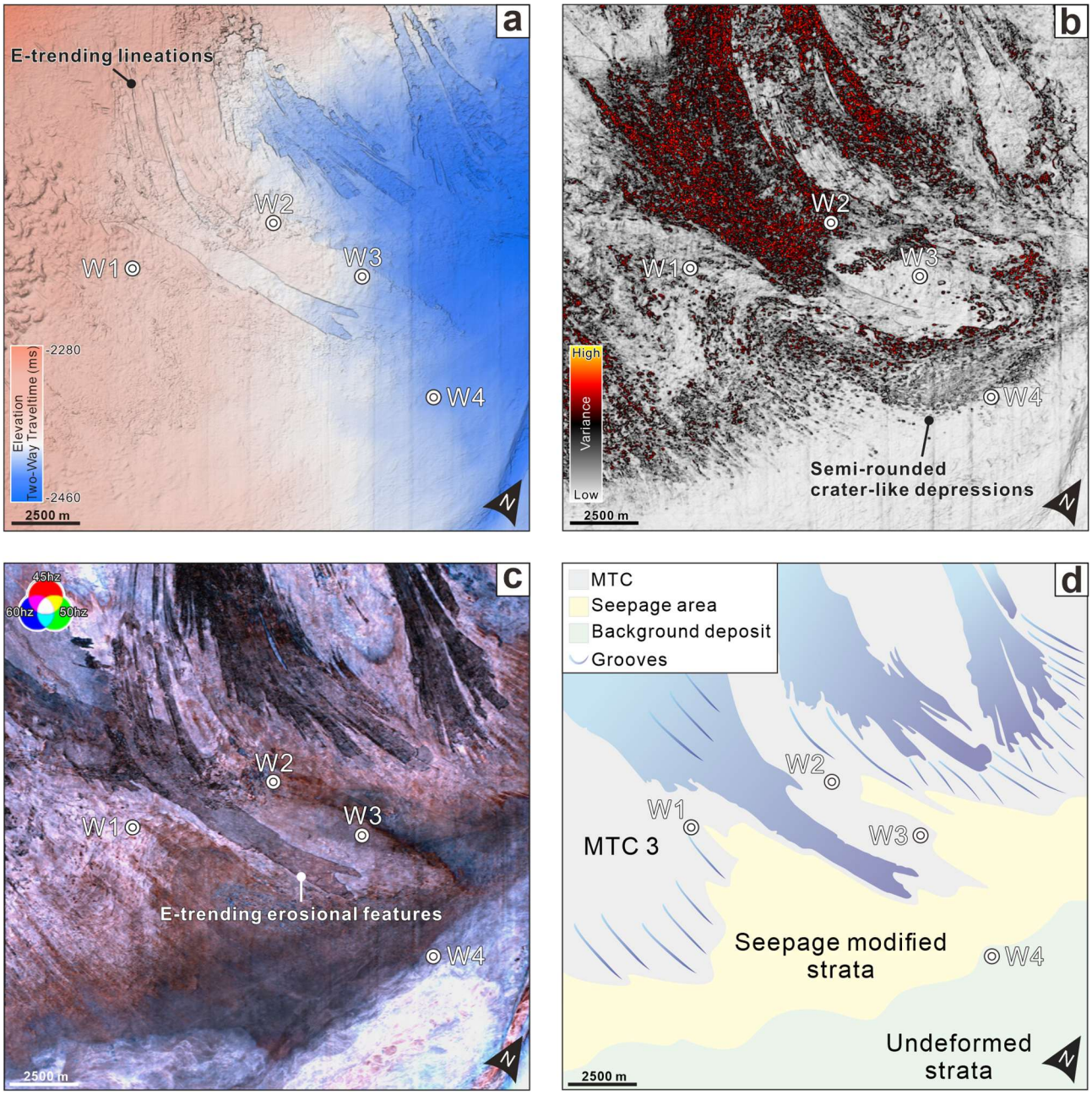
a
E-trending lineations
W1
W2
W3
W4
Elevation Two-Way Traveltime (ms)
-2280
-2460
2500 m
b
W1
W2
W3
W4
High
Variance
Low
Semi-rounded crater-like depressions
2500 m
c
45hz
60hz
50hz
W1
W2
W3
W4
E-trending erosional features
2500 m
d
MTC
Seepage area
Background deposit
Grooves
W1
W2
W3
W4
MTC 3
Seepage modified strata
Undeformed strata
2500 m

Figure 5

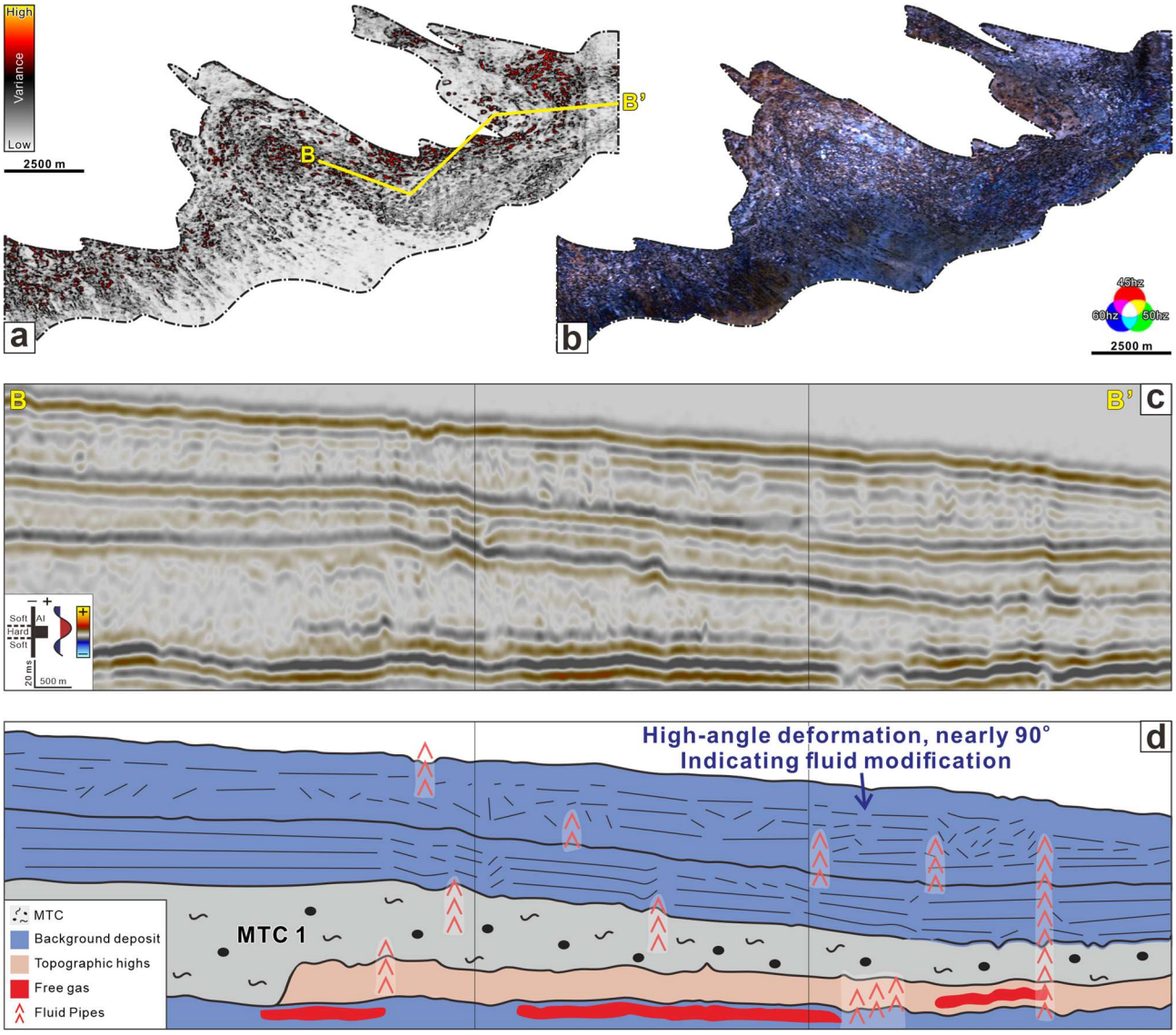

892

893 Figure 6

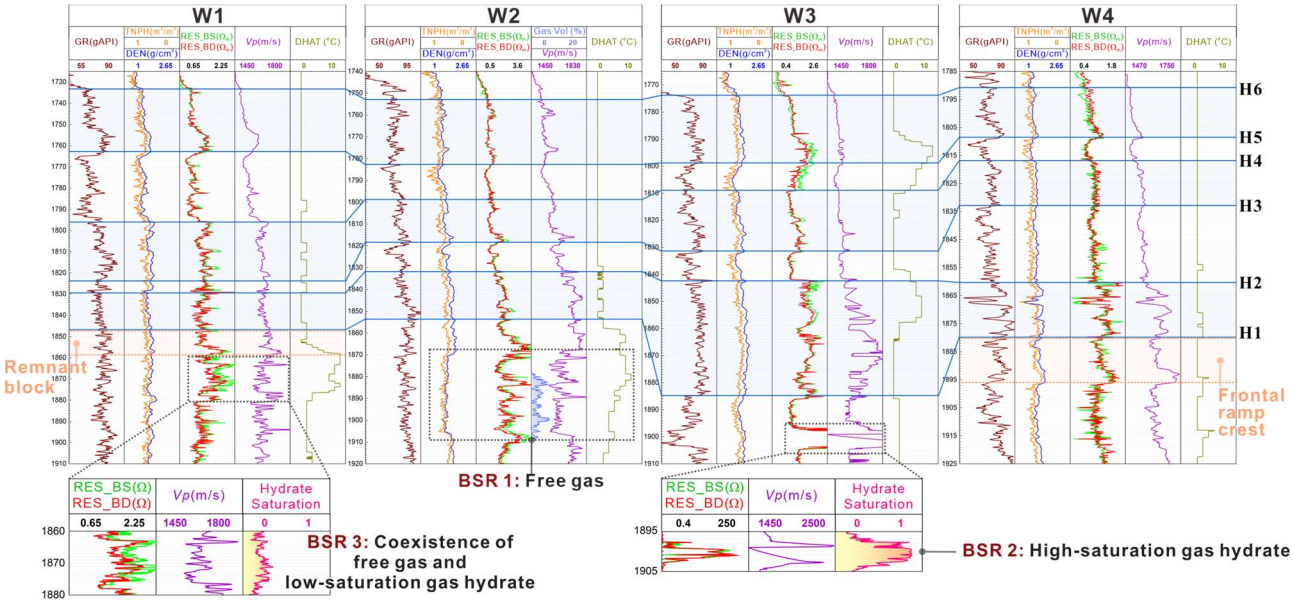
W1
W2
W3
W4
GR(gAPI)
TNPH(m³/m³)
DEN(g/cm³)
RES_BS(Ω·m)
RES_BD(Ω·m)
Vp(m/s)
DHAT (°C)
Gas Vol (%)
H6
H5
H4
H3
H2
H1
Remnant block
Frontal ramp crest
RES_BS(Ω)
RES_BD(Ω)
Hydrate Saturation
BSR 1: Free gas
BSR 3: Coexistence of free gas and low-saturation gas hydrate
BSR 2: High-saturation gas hydrate

Figure 7

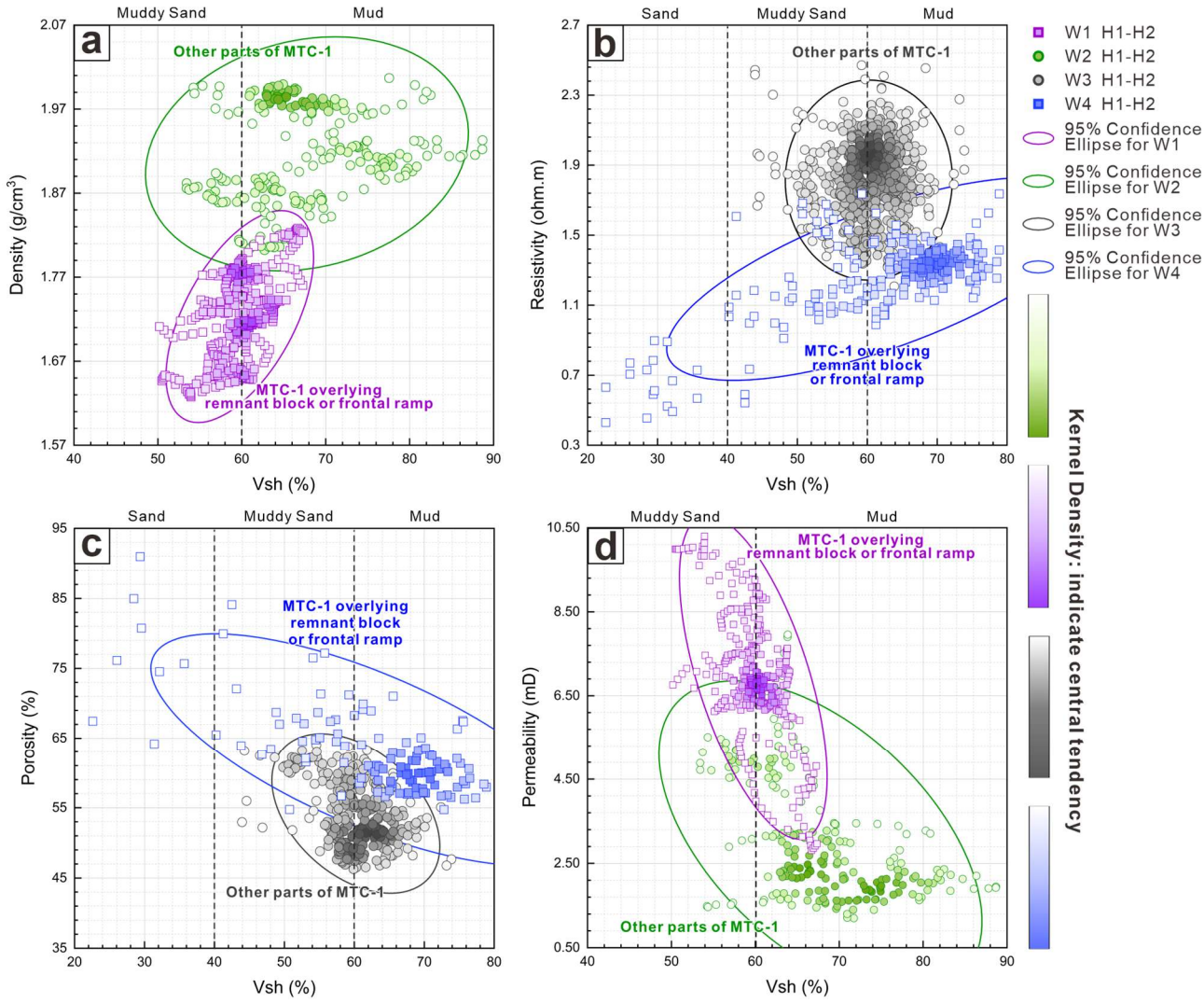
a
Muddy Sand
Mud
Other parts of MTC-1
MTC-1 overlying remnant block or frontal ramp
Density (g/cm3)
Vsh (%)
b
Sand
Muddy Sand
Mud
Other parts of MTC-1
MTC-1 overlying remnant block or frontal ramp
Resistivity (ohm.m)
Vsh (%)
c
Sand
Muddy Sand
Mud
MTC-1 overlying remnant block or frontal ramp
Other parts of MTC-1
Porosity (%)
Vsh (%)
d
Muddy Sand
Mud
MTC-1 overlying remnant block or frontal ramp
Other parts of MTC-1
Permeability (mD)
Vsh (%)
W1 H1-H2
W2 H1-H2
W3 H1-H2
W4 H1-H2
95% Confidence Ellipse for W1
95% Confidence Ellipse for W2
95% Confidence Ellipse for W3
95% Confidence Ellipse for W4
Kernel Density: indicate central tendency

Figure 8

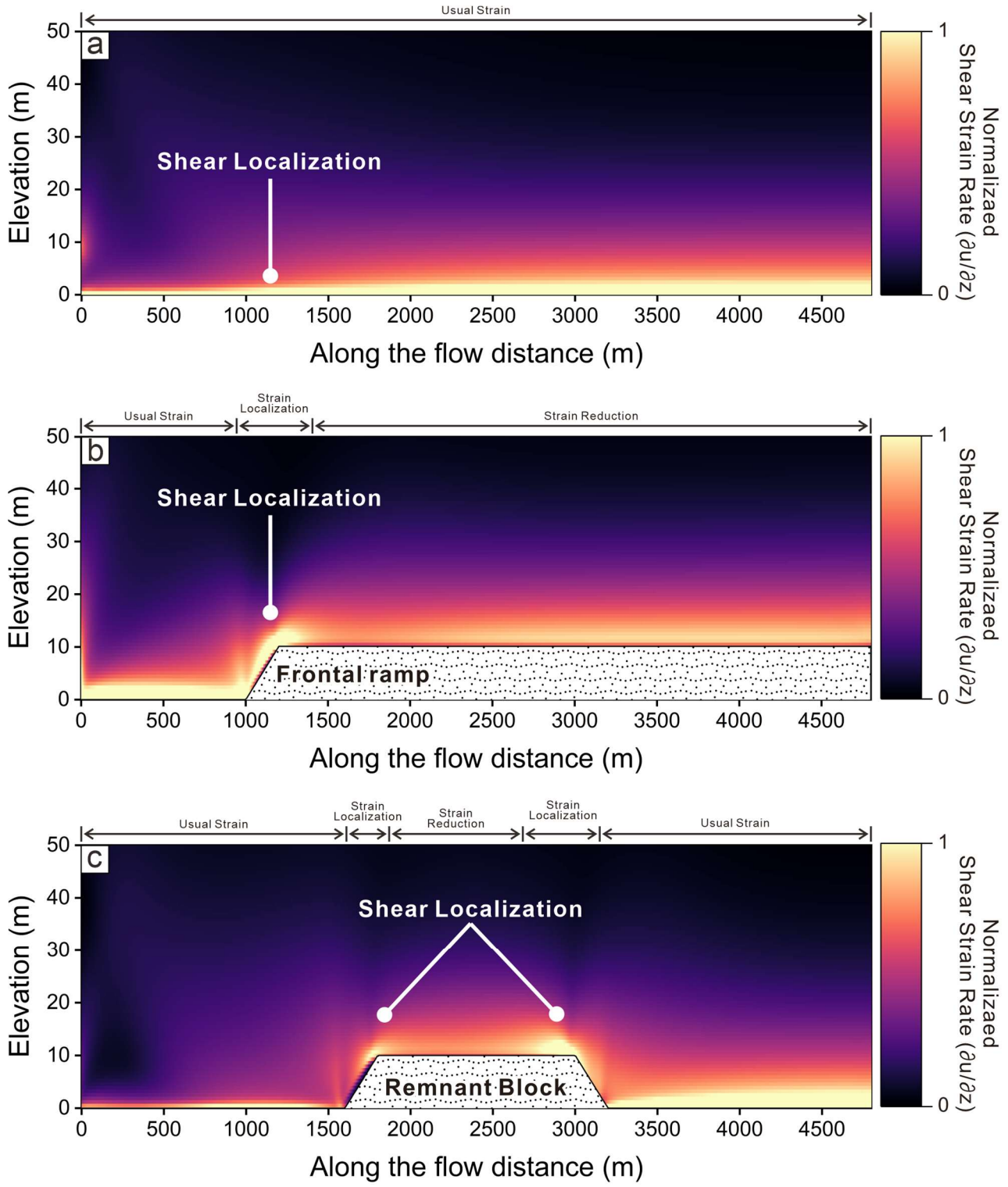

898

899 Figure 9

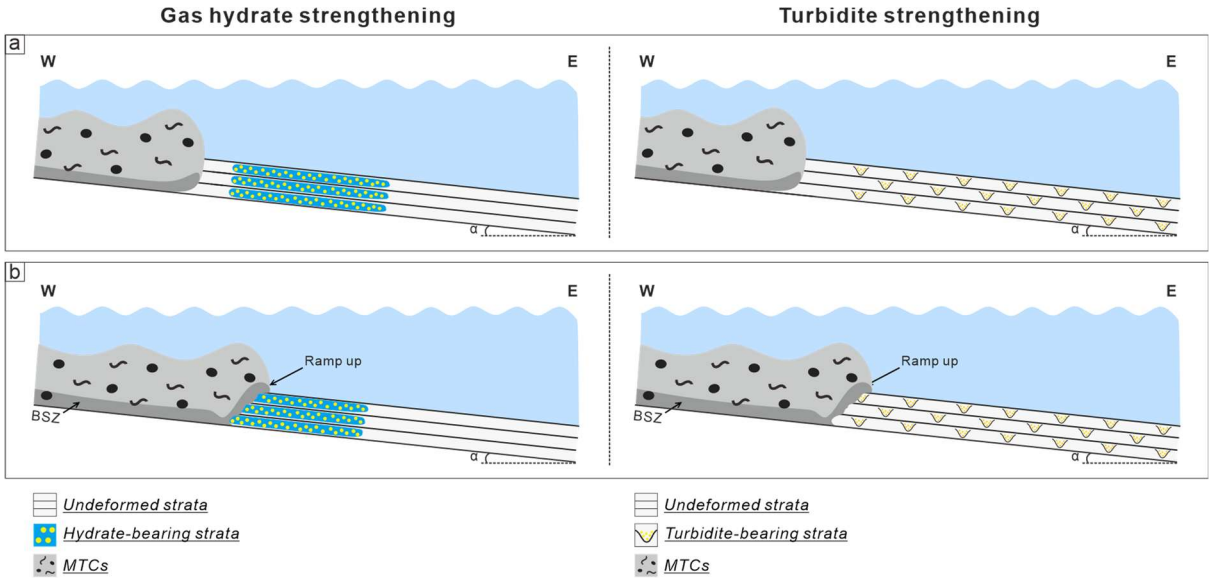
Gas hydrate strengthening
Turbidite strengthening
a
b
W
E
Ramp up
BSZ
α
Undeformed strata
Hydrate-bearing strata
MTCs
Undeformed strata
Turbidite-bearing strata
MTCs

Figure 10

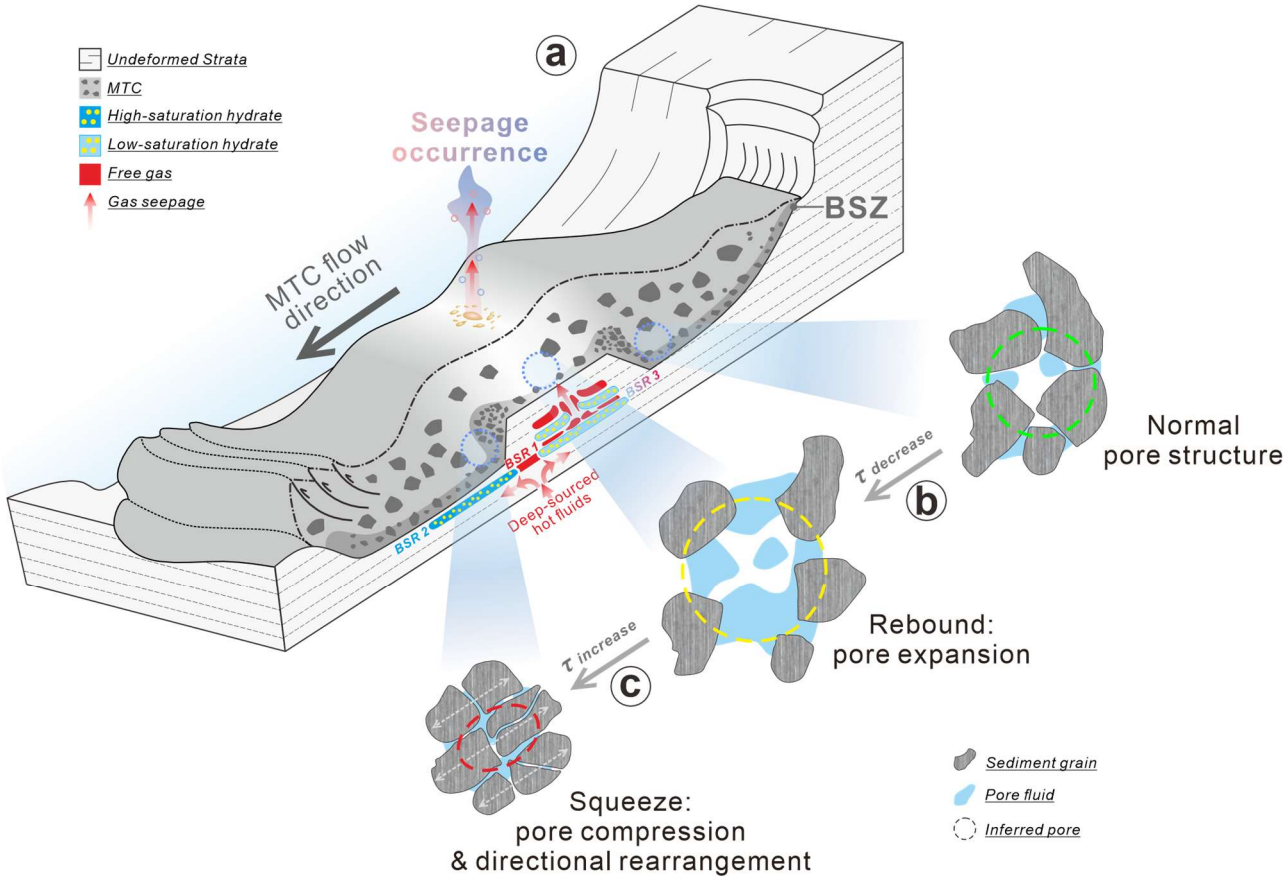

902

903 Figure 11

904

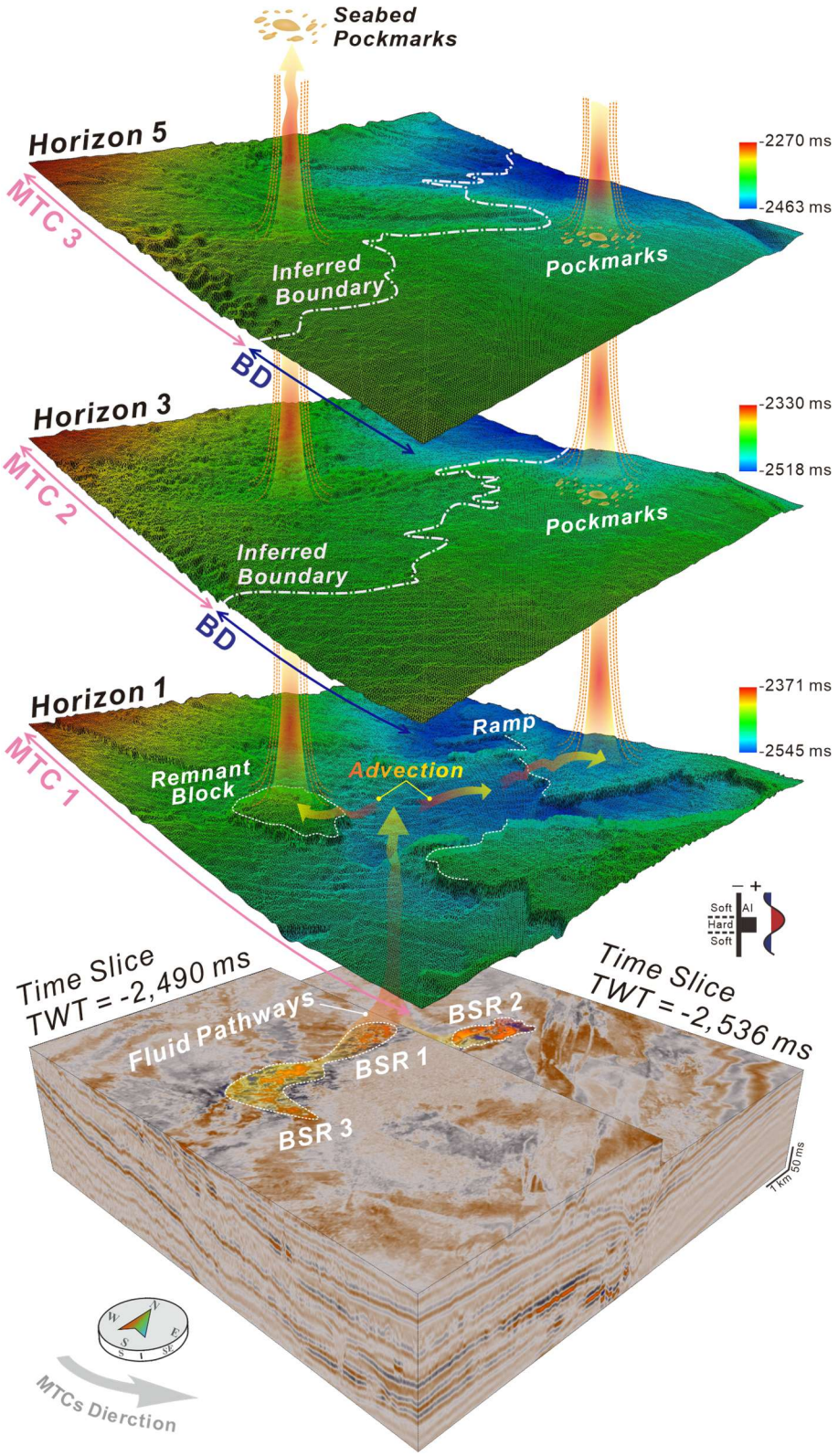

905

906 Figure 12

907

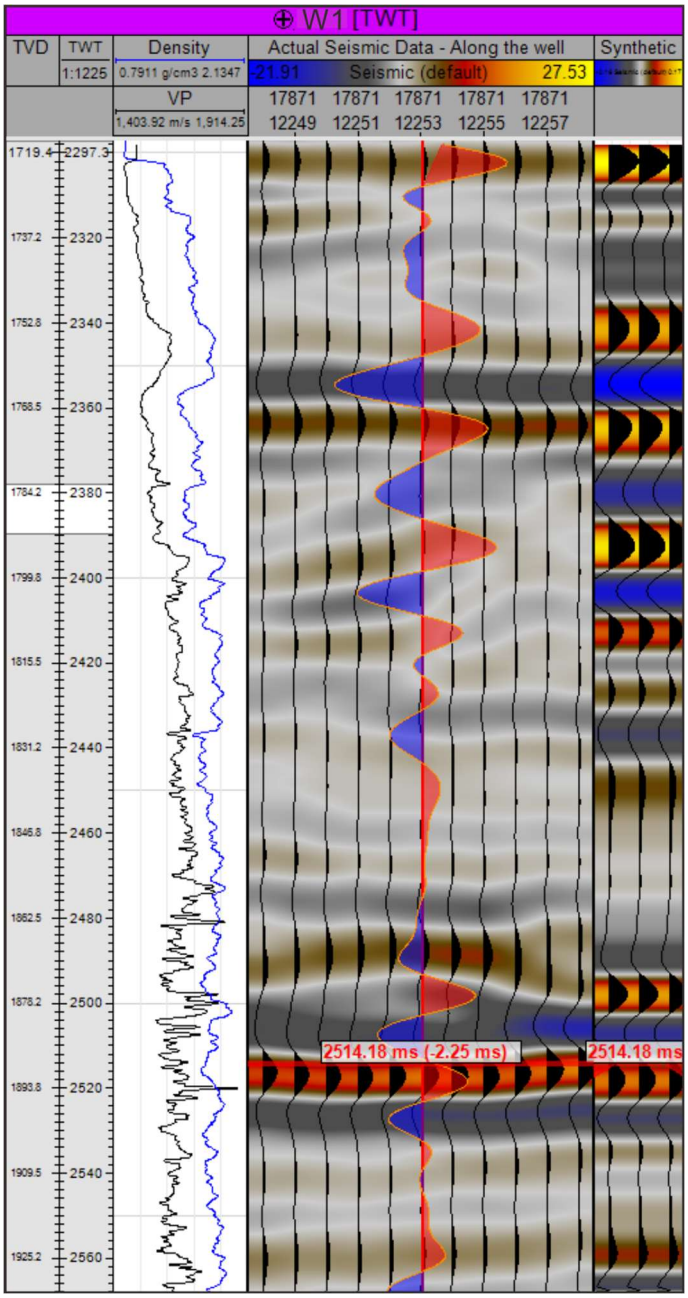

908

909 Figure A1